NASA
Technical Memorandum 84553

AVRADCOM
Technical Report 82-B-6

Reduction of High-Speed Impulsive Noise by Blade Planform Modification of a Model Helicopter Rotor

David A. Conner and Danny R. Hoad
Structures Laboratory
AVRADCOM Research and Technology Laboratories
Langley Research Center
Hampton, Virginia

National Aeronautics
and Space Administration

Scientific and Technical
Information Branch

1982

SUMMARY

An experiment has been performed to investigate the reduction of high-speed impulsive noise by using an advanced main rotor system for the UH-1H helicopter. The advanced rotor system had a tapered blade planform compared with a rectangular planform for the standard rotor system. Models of both the advanced main rotor system and the UH-1H standard main rotor system were tested at 1/4 scale in the Langley 4- by 7-Meter Tunnel (formerly the Langley V/STOL Tunnel) using the general rotor model system (GRMS). Tests were conducted throughout the UH-1H velocity range (80 to 110 knots) for which this type of noise is of concern. The tunnel was operated in the optional open-throat configuration, with acoustical treatment applied to the ceiling and floor to improve the acoustic characteristics of the test chamber. In-plane acoustic measurements of the high-speed impulsive noise demonstrated that the advanced rotor system on the UH-1H helicopter reduced the high-speed impulsive noise by up to 20 dB, with a reduction in overall sound pressure level of up to 6 dB.

INTRODUCTION

Aerodynamically generated noise from a helicopter can be broken down into several categories not totally independent of each other. Of most concern is impulsive noise, or blade slap, because of its relative loudness (refs. 1 to 3). Impulsive noise, as reported in reference 4, can be generated in the following two ways: (1) high-speed impulsive (HSI) noise due to shock-wave formation and collapse on the advancing blade tip; and (2) blade-vortex interaction (BVI) impulsive noise due to the impulsive change in blade loading during blade- and trailing-vortex interaction which occurs in low-power descending flight or maneuvers. This paper is concerned only with HSI noise.

Two different theories have been developed to account for the generation of HSI noise. One theory (ref. 5) correlates compressibility effects related to high rotor blade-tip speeds and observed blade-tip shock-wave formations with observed HSI noise pressure-time histories. Another theory (ref. 6) models the HSI noise production by the pressure disturbance of the fluid medium caused by the motion of the blade (rotor blade thickness effect). Both theories predict that the HSI noise has the distinctive characteristic of being directional towards the forward region of flight with the peak pressure in the plane of the rotor. Because helicopters generally operate at low altitudes, most surrounding land surface areas (except those immediately under the helicopter) are subjected to this in-plane HSI noise. If the aircraft is operating in a combat zone and the element of surprise is desired, any reduction of this HSI noise would reduce the aural detectability of the aircraft.

Since the original design, the gross weight of the various models of the UH-1H helicopter has increased substantially. This increase in gross weight has necessitated a corresponding increase in rotor thrust capability. A new blade design has been developed for which performance and HSI-noise prediction routines indicated improvements over the standard blade (refs. 7 and 8). The planform of this design is tapered, and the thickness is reduced at the tip compared with the current UH-1H rotor blade design. The reduction of blade-tip thickness was expected to reduce HSI noise. The noise reduction potential of the new blade design is therefore investigated experimentally in this study. The experimental results are presented to com-

pare the HSI noise produced by a 1/4-scale model of the UH-1H with advanced rotor blades with that produced by a 1/4-scale model with standard rotor blades.

SYMBOLS

A_1 first harmonic of lateral cyclic blade pitch, deg

a_o rotor coning angle, fixed at 2.75°

a_{1_s} first harmonic of longitudinal flapping, deg

B_1 first harmonic of longitudinal cyclic blade pitch, deg

b_{1_s} first harmonic of lateral flapping, deg

C_Q rotor torque coefficient, $\frac{\text{Rotor torque}}{\rho\pi R^3(\Omega R)^2}$

C_T rotor thrust coefficient, $\frac{\text{Rotor thrust}}{\rho\pi R^2(\Omega R)^2}$

c standard rotor system blade chord, 0.1334 m

D rotor drag, dynes

F frequency, Hz

L rotor lift, dynes

M_T advancing-blade-tip Mach number, $\frac{V_\infty + \Omega R}{\text{Local speed of sound}}$

P_p peak negative impulse pressure, dynes/cm^2

R rotor radius, 1.829 m

V_T rotor blade-tip speed, m/sec

V_∞ free-stream velocity, knots

x,y,z coordinates for microphone locations in tunnel, m

α angle of attack of rotor shaft, deg

α_{TPP} rotor tip-path-plane angle of attack, referenced to tunnel geometric centerline, deg

γ rotor descent angle, $\tan^{-1}(D/L)$

θ_c rotor collective control angle, deg

μ advance ratio, V_∞/V_T

ρ local free-stream density, kg/m^3

τ reference impulse width

Ω rotor angular rotational velocity, rpm

Abbreviations:

ARS advanced rotor system

BVI blade-vortex interaction

HSI high-speed impulsive

OASPL overall sound pressure level, dB (re 0.0002 $dynes/cm^2$)

rpm revolutions per minute

SPL sound pressure level, dB (re 0.0002 $dynes/cm^2$)

SRS standard rotor system

HELICOPTER MODEL, TEST FACILITY, AND INSTRUMENTATION

Helicopter Model

This test was conducted in the Langley 4- by 7-Meter Tunnel (formerly the Langley V/STOL Tunnel) using the general rotor model system (GRMS) as described in reference 9. The 1/4-scale model of the UH-1H fuselage was designed to enclose the basic model, transmission, and controls for the rotor system. A sketch of the helicopter model is shown in figure 1. Two six-component strain-gage balances were used for this test, one supporting the fuselage shell and one supporting the rotor system including the actuators, electric drive motor, and transmission. Aerodynamic performance measurements presented herein were obtained from the rotor balance and referenced to the shaft axis system. (See ref. 7.)

Two different rotor systems were tested in this test, each mounted on the same geometrically scaled version of the UH-1H rotor hub. One rotor system used the standard, or baseline, rotor blades, which were geometrically and dynamically scaled models of the current UH-1H rotor blades. This system is hereafter referred to as the standard rotor system (SRS). These blades were made of a fiberglass/Kevlar[1] composite having a graphite/epoxy composite structural torque box. The aerodynamic contours were formed by means of an external fiberglass/epoxy shell with a Nomex[2] honeycomb core in the trailing edge. The other rotor system tested incorporated a totally different blade planform and is referred to as the advanced rotor system (ARS). These advanced rotor blades had a wider root chord compared with the standard rotor blades, with a 3 to 1 taper ratio beginning at the 50 percent radius. Advanced

---

[1]Kevlar: Registered trade name of E. I. du Pont de Nemours & Co., Inc.
[2]Nomex: Registered trade name of E. I. du Pont de Nemours & Co., Inc.

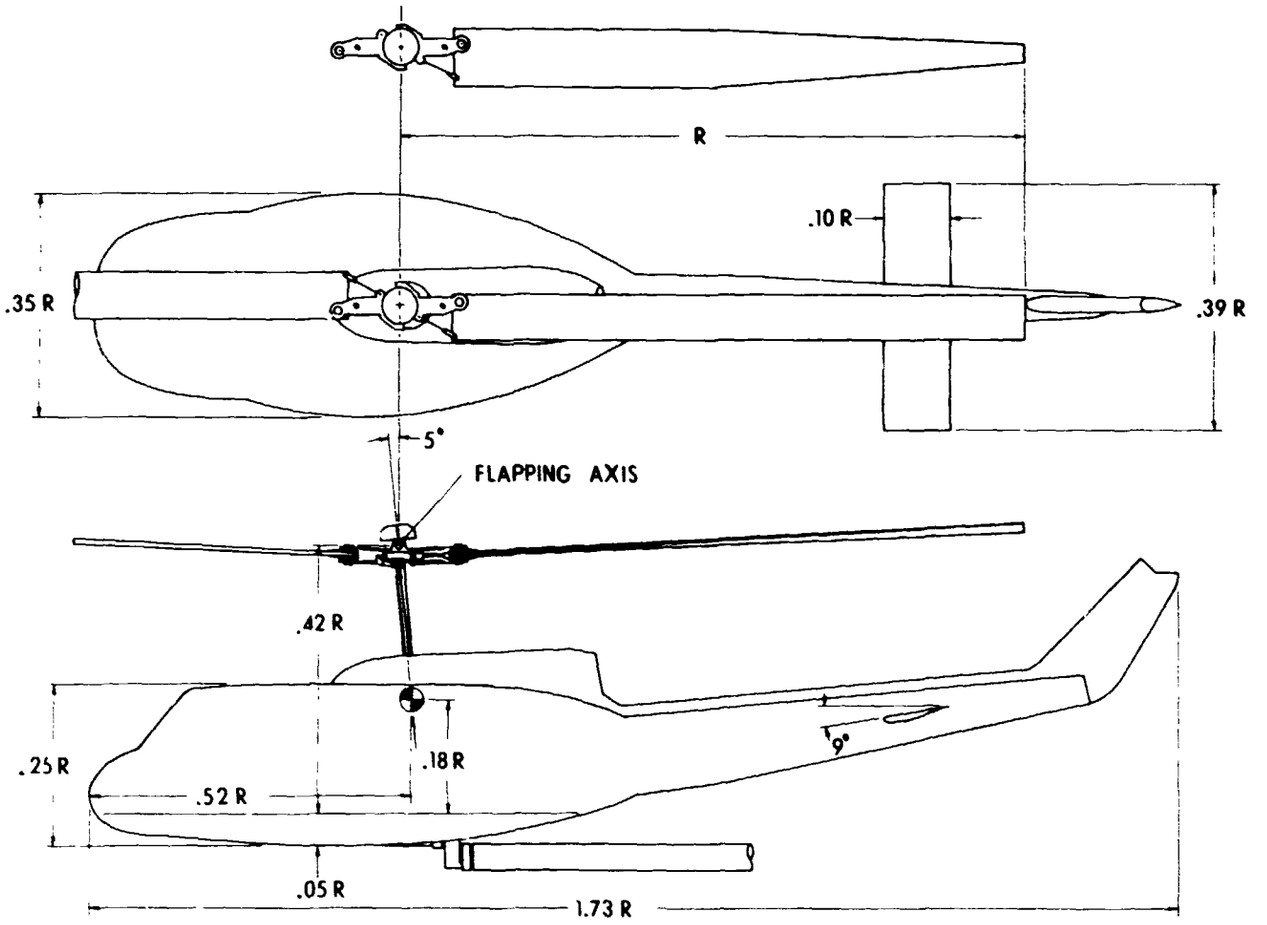

Figure 1.- Sketch of UH-1H helicopter model tested.

rotorcraft airfoils (ref. 10) were used, with thickness ratios ranging from 12 percent inboard to 8 percent at the tip. Construction was similar to that of the standard rotor blades with the exception of a Styrofoam[3]/balsa trailing-edge core. A sketch of the two different rotor blade designs tested is shown in figure 2; their dimensional characteristics are presented in table I.

The model has a teetering-type rotor hub. Collective and cyclic pitches on the blades were controlled by a swash plate driven by remotely controlled actuators and were measured directly at the rotor hub. Rotor-system teetering measurements were made at the teetering axis. A 67-kW electric motor operating through a transmission drove the rotor. An optical encoder provided both rotational-speed measurement and azimuthal indexing of the rotor system.

---

[3]Styrofoam: Registered trade name of Dow Chemical Co.

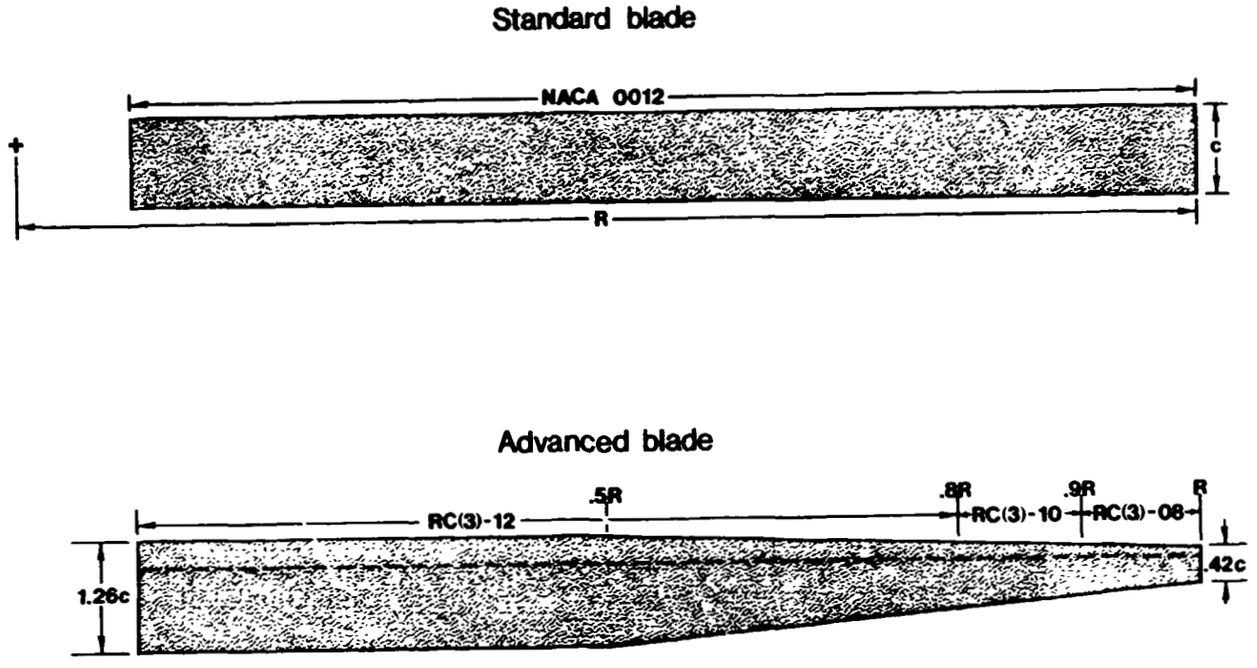

Figure 2.- Geometric comparison of standard and advanced rotor blades.

TABLE I.- ROTOR CHARACTERISTICS

Number of blades	2
Airfoil section:	
Standard blade	NACA 0012
Advanced blade	RC(3)-12, RC(3)-10, RC(3)-08
Radius, m	1.829
Blade chord:	
Standard blade, m	0.1334
Advanced blade, m	0.0560 to 0.1681
Twist:	
Standard blade, deg	-10.9
Advanced blade, deg	-14.0
Planform solidity:	
Standard blade	0.04642
Advanced blade	0.04863
Root cutout, m	0.1554

Wind-Tunnel Facility

This test was conducted in the Langley 4- by 7-Meter Tunnel operated in the open-throat configuration (figs. 3 and 4). The dimensions of the rectangular jet

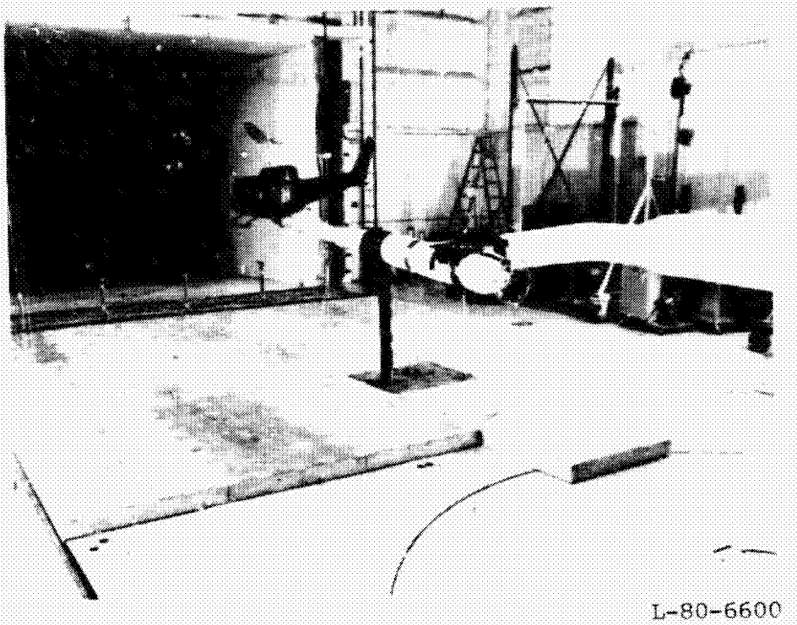

L-80-6600

Figure 3.- Rear quarter-view of UH-1H helicopter model in Langley 4- by 7-Meter Tunnel with acoustic treatment and microphones installed.

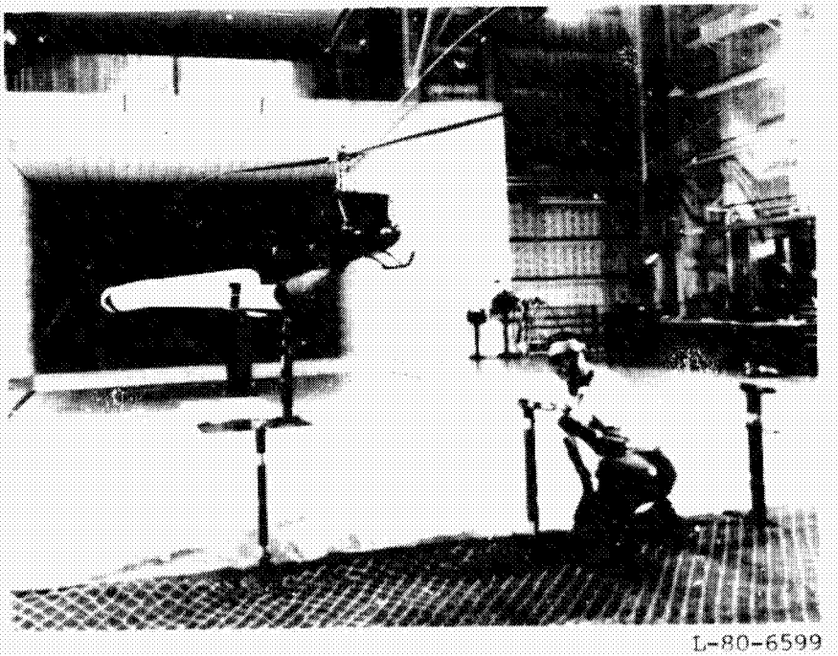

L-80-6599

Figure 4.- Front quarter-view of UH-1H helicopter model in Langley 4- by 7-Meter Tunnel with acoustic treatment and microphones installed.

entrance to the test chamber are 4.42 m high by 6.63 m wide. The ceiling height in the open-throat configuration was approximately 7.50 m above the test chamber floor. The model was supported in the wind-tunnel test section by a unique three-joint sting which allowed pitch and yaw control to ±45° about a fixed point on the model. This three-joint sting was mounted on a model support system which allowed height control as well as limited additional pitch and yaw control.

In order to obtain realistic free-field noise measurements in this facility, acoustic treatment was installed on the tunnel floor and ceiling. Fiberglass-filled aluminum panels 12.7 cm thick were installed on the floor directly under and forward of the model (see figs. 3 and 4) for a semirigid floor to facilitate periodic maintenance and modifications to the model. Open-cell polyurethane foam 10.2 cm thick was installed on the floor directly ahead of the aluminum panels and overhead on the surface of the raised ceiling. (See fig. 5). An evaluation of the effectiveness of this ceiling and floor treatment is reported in reference 11.

Instrumentation

The acoustic transducers used for this investigation were 1.27-cm-diameter condenser microphones fitted with standard nose cones. Five far-field microphones were positioned upstream of the model and three near-field microphones were attached directly to the model fuselage. (See figs. 3 to 5.) A sketch of the model installed in the tunnel with floor treatment and microphone locations is presented in figure 5. Near-field microphones 1, 2, and 3 and far-field microphones 6, 7, and 8 were strategically mounted on and upstream of the model to detect specific types of noise other than HSI noise. Far-field microphones 4 and 5 were mounted upstream of the model as far as possible from the rotor (1.10R) but still in the free-field environment of the facility. These microphones were in the rotor tip-path plane, where HSI noise has been shown to be maximum (ref. 12). These in-plane microphones were mounted approximately 33° to the right and to the left of the tunnel centerline as measured from the rotor hub, so that the support fairing wake was outside the rotor disk. Only data from microphones 4 and 5 are presented in this paper. Based on the coordinate system presented in figure 5, microphone 4 was located at $x = -3.27$ m, $y = 2.16$ m, and $z = -0.17$ m, and microphone 5 was located at $x = -3.28$ m, $y = -2.23$ m, and $z = -0.17$ m. The origin of this coordinate system was a point in space located at the rotor hub when the model was at a fuselage angle of attack of 0°. Signals from each microphone were fed through an amplifier/attenuator into a 14-channel, frequency-modulated (FM) tape recorder operating at a tape speed of 76.2 cm/sec. Blade azimuth and time code were recorded simultaneously with the microphone data.

OPERATING PROCEDURES AND DATA REDUCTION

Operating Procedures

High-speed impulsive noise has been shown to propagate towards the forward region of flight, with the peak pressure in the plane of the rotor. Therefore, it was appropriate to position the microphones in the plane of the rotor. The procedure used to establish each flight condition at a fixed rotor rotational velocity (1300 rpm) was to operate the tunnel and the model at the desired simulation condition and determine the rotor tip-path-plane angle of attack α_{TPP}. After shutting the tunnel down, the microphones were manually moved to be directly in the plane of the rotor. The tunnel and the model were then brought back to the proper

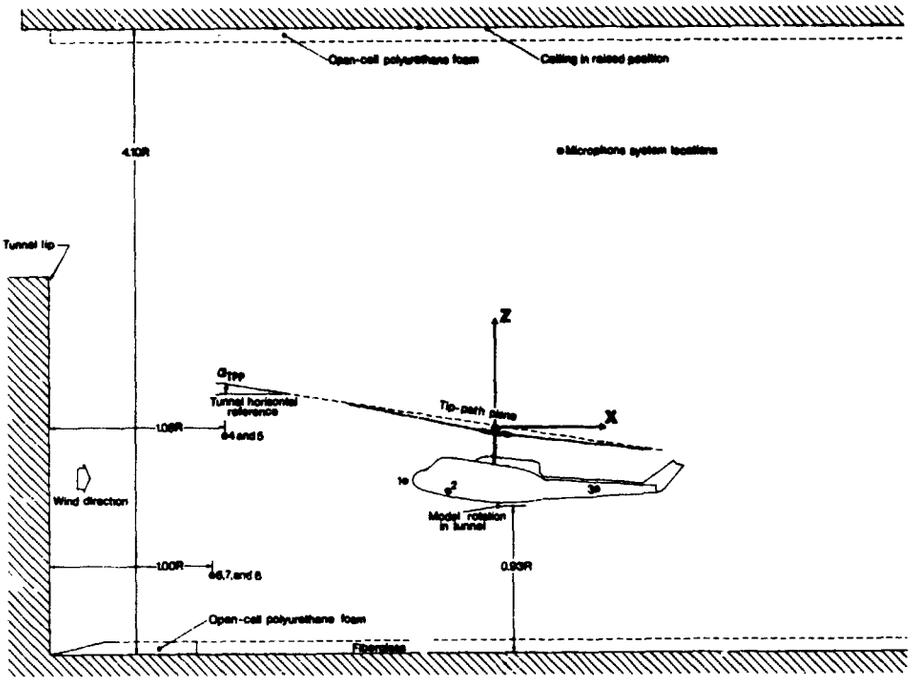

(a) Side view.

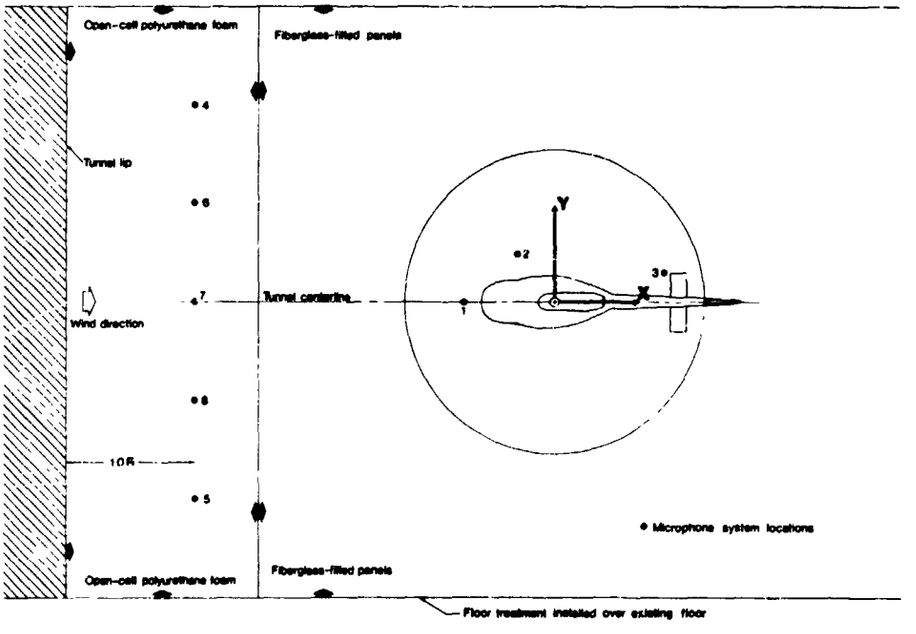

(b) Top view.

Figure 5.- Relative position of components in acoustic test of UH-1H helicopter model.

flight condition and approximately 20 sec of information from the microphones was recorded on tape. A rotor lift coefficient of 0.0031 (defined as rotor lift nondimensionalized by the product of rotor disk area, hover blade-tip-speed squared, and local free-stream density) was maintained throughout the HSI-noise portion of the acoustic test. At each simulated forward-flight speed desired, estimates of flight-scaled rotor-shaft angle and lateral flapping were used to set the model conditions in the wind tunnel. Rotor cyclic and collective pitch controls were adjusted to obtain these values and to trim the rotor thrust vector to balance the drag of the fuselage. For each data point taken, corresponding model and tunnel information were recorded simultaneously with the acoustic information using the tunnel data acquisition system. The full aerodynamic-performance characteristics for the speed range of concern (80 to 110 knots) are listed in table II, and the sign convention used for these parameters is presented in figure 6. At each tunnel speed tested, background noise measurements were made with the blades off and the rotor hub turning at the proper test conditions.

TABLE II.- ROTOR OPERATING CONDITIONS

[See fig. 6 for axis convention]

Run	Point	V_∞, knots	α, deg	α_{TPP}, deg	θ_c, deg	A_1, deg	B_1, deg	a_{1_s}, deg	b_{1_s}, deg	γ, deg	μ	C_T	C_Q
Standard rotor system													
167	2152	80.5	-3.76	-1.69	5.21	-2.41	0.16	1.97	-1.23	0.27	0.166	0.0031	0.00010
168	2155	85.5	-3.74	-1.81	5.34	-2.36	.52	1.82	-1.25	.23	.177	.0031	.00010
169	2158	90.1	-3.89	-2.05	5.40	-2.26	.74	1.74	-1.20	.14	.186	.0031	.00011
170	2162	95.0	-3.87	-2.10	5.52	-2.24	1.04	1.67	-1.20	.14	.196	.0031	.00011
171	2164	100.6	-3.85	-2.25	5.65	-2.20	1.47	1.50	-1.18	.12	.208	.0031	.00011
171	2165	100.3	-3.84	-2.22	5.66	-2.20	1.46	1.53	-1.17	.09	.207	.0031	.00011
172	2169	105.5	-3.82	-2.30	5.77	-2.18	1.77	1.43	-1.16	.11	.218	.0032	.00012
173	2172	110.6	-3.81	-2.53	5.93	-2.05	2.25	1.18	-1.14	.13	.229	.0031	.00012
Advanced rotor system													
202	2603	80.0	-3.79	-1.78	7.44	-3.19	0.55	1.89	-1.54	-0.51	0.166	0.0032	0.00009
203	2607	85.1	-3.77	-1.94	7.50	-3.16	.92	1.70	-1.60	-.35	.176	.0032	.00009
205	2614	90.0	-3.76	-2.10	7.60	-2.93	1.12	1.54	-1.48	-.51	.186	.0032	.00009
206	2618	95.1	-3.87	-2.12	7.73	-2.86	1.24	1.63	-1.45	.01	.197	.0032	.00009
207	2620	100.0	-3.85	-2.36	7.92	-2.78	1.75	1.36	-1.48	.03	.207	.0032	.00010
207	2621	100.1	-3.85	-2.33	7.92	-2.78	1.75	1.40	-1.49	.19	.207	.0032	.00010
209	2628	106.0	-3.87	-2.92	8.33	-2.64	2.77	.83	-1.47	-1.08	.219	.0032	.00011
210	2633	110.2	-3.83	-2.64	8.36	-2.49	2.60	1.07	-1.38	-.21	.228	.0032	.00011

Before and after the tests, "pink" and "white" noise signals were recorded to verify that the complete acoustic system (excluding the microphones) had a flat frequency response over the range of interest (30 to 8000 Hz). All microphones were calibrated with a 124-dB pistonphone at 250 Hz before and after each series of tests.

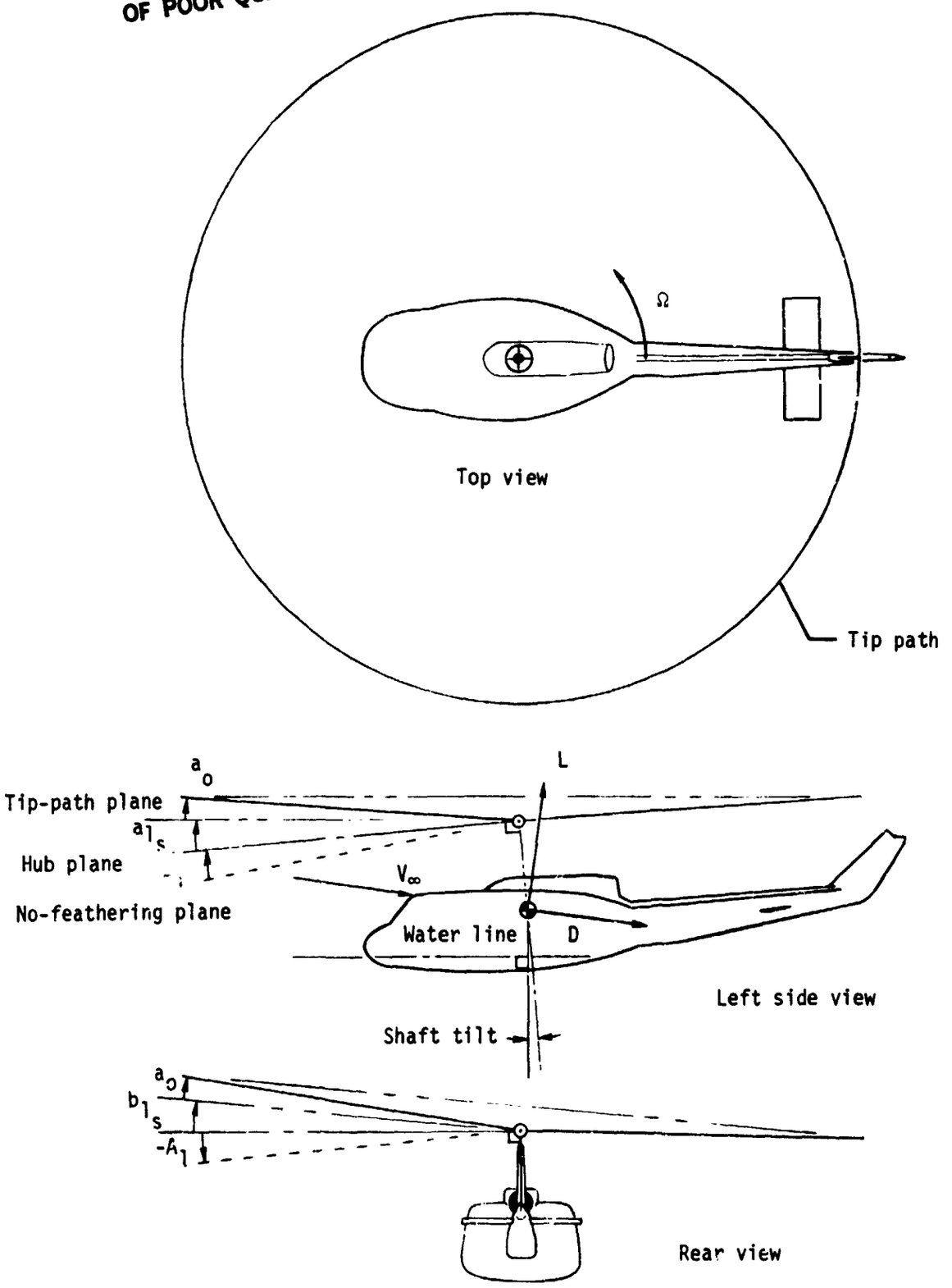

Figure 6.- Sign convention for aerodynamic performance characteristics.

Data Reduction

Corrections for jet-boundary and blockage effects were handled on-line to ensure proper helicopter model operating conditions. The corrections were computed in greater detail off-line for complete aerodynamic-performance data reduction. The method of applying these corrections is described in reference 13.

Each acoustic record was digitized at a rate of approximately 22 118 samples per second. The data were then processed through a low-pass filter of 10 000 Hz to prevent aliasing. A once-per-revolution electronic pulse generated by the optical encoder within the model was used as a trigger for precise digitization so that 1024 samples were obtained during each revolution. The time-domain data presented in this paper were obtained by ensemble averaging 40 rotor revolutions for all tunnel speeds except 110 knots, which was averaged using 6 rotor revolutions. This ensemble averaging was done to enhance periodic-noise components. These acoustic data were also analyzed using a fast-Fourier-transform technique with a "boxcar windowing" function for maximum resolution (ref. 14). The bandwidth of these data was 21.65 Hz, with a blade-passage frequency of 43.3 Hz. Eighty degrees of freedom were obtained by averaging 40 spectral calculations of 1 revolution. Based on the chi-square distribution of the variance for 80-percent confidence, the digital-analysis process yielded a variability of 20 percent in the spectral-power estimates.

DISCUSSION OF RESULTS

Data Repeatability

In order to confirm that the data presented in this paper are representative samples of the overall data collected during this test, a data repeatability comparison for V_∞ = 100 knots is presented in figure 7. Figures 7(a), 7(c), 7(e), and 7(g) show comparisons of random 1-revolution samples, whereas figures 7(b), 7(d), 7(f), and 7(h) present comparisons of the periodic-noise sources as a 40-revolution average. The two different sets of data which are compared throughout figure 7 were obtained as two separate data points taken back to back without changing any model or tunnel parameters.

As expected, the random-noise comparisons of the one-revolution-sample plots are not identical, although they are very similar. The negative HSI-noise spikes show very good repeatability when they are not contaminated by background noise (which is not related to rotor noise).

The periodic-noise comparisons of the 40-revolution-average plots show very good comparisons of the noise level generated by the rotor but not related to the HSI-noise waveform, whereas comparisons of the negative HSI-noise spike are nearly identical. Even for the case of the ARS at microphone 5 (fig. 7(h)), in which no HSI-noise spike is evident and the vertical scale spans only 200 dynes/cm^2, a remarkably good comparison was obtained. This indicates repeatable periodic noise exists other than that due to HSI noise.

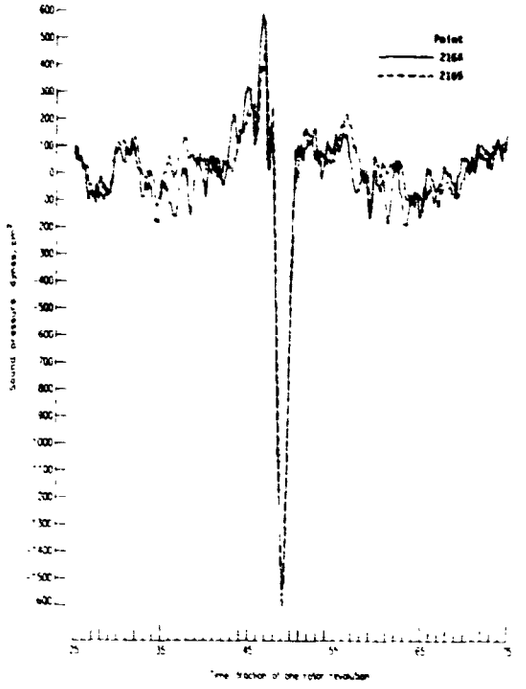

(a) Standard rotor system; 1-revolution sample from microphone 4.

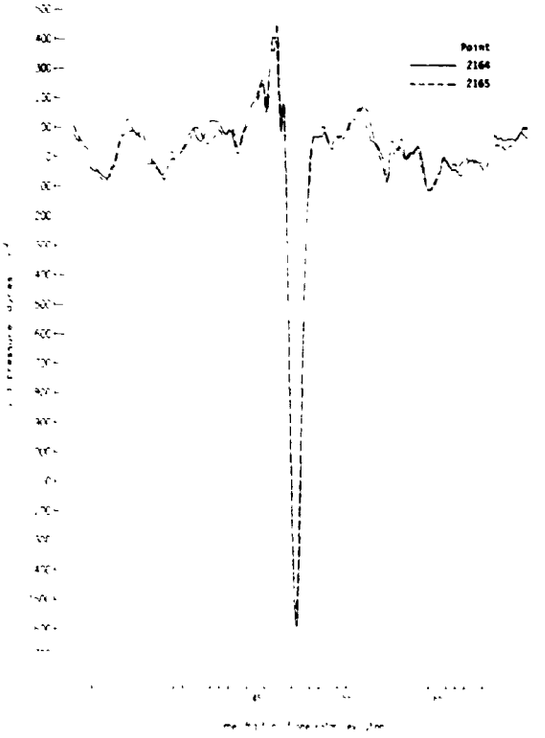

(b) Standard rotor system; 40-revolution average from microphone 4.

Figure 7.- Data repeatability comparison for V_∞ = 100 knots.

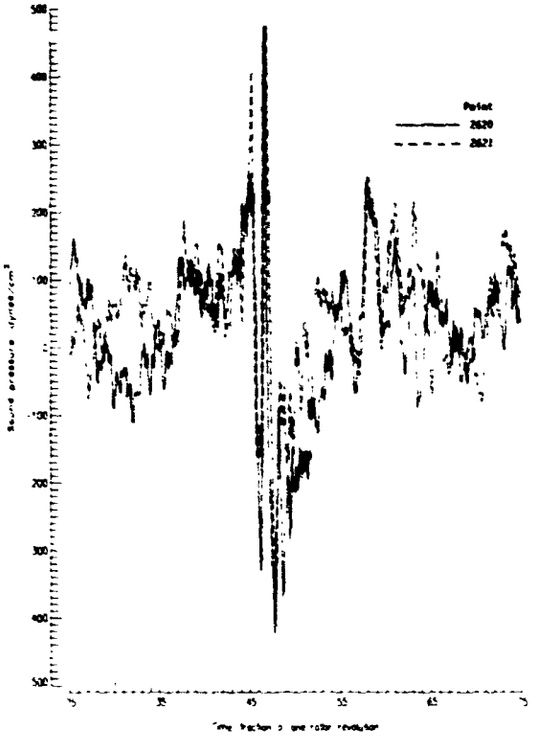

(c) Advanced rotor system; 1-revolution sample from microphone 4.

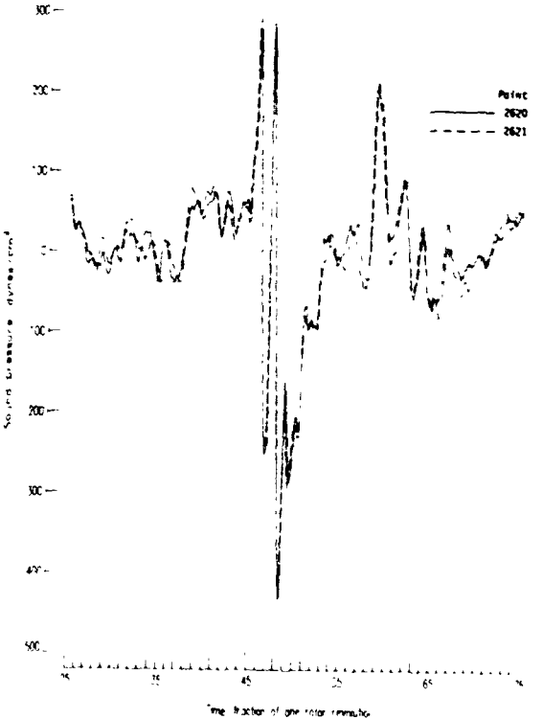

(d) Advanced rotor system; 40-revolution average from microphone 4.

Figure 7.- Continued.

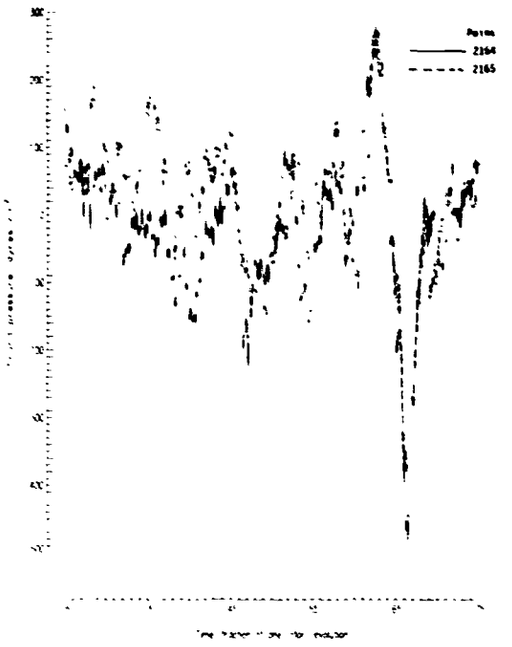

(e) Standard rotor system; 1-revolution sample from microphone 5.

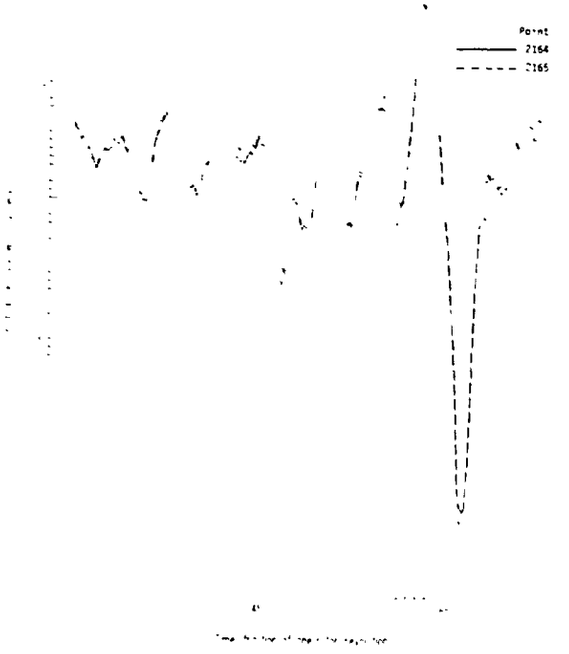

(f) Standard rotor system; 40-revolution average from microphone 5.

Figure 7.- Continued.

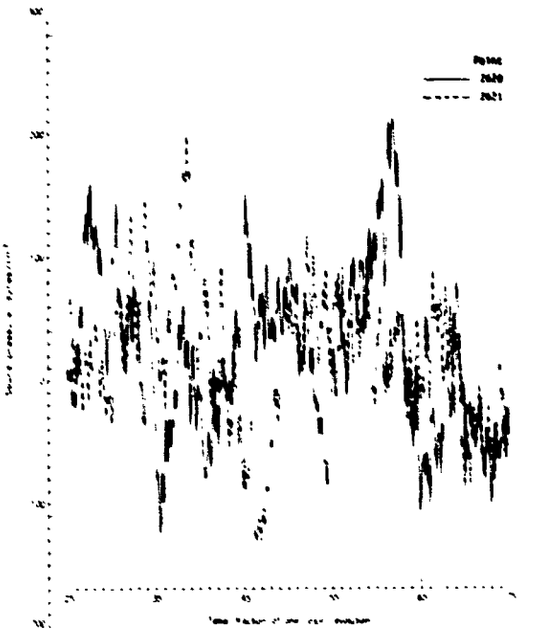

(c) Advanced rotor system; 1-revolution sample from microphone 5.

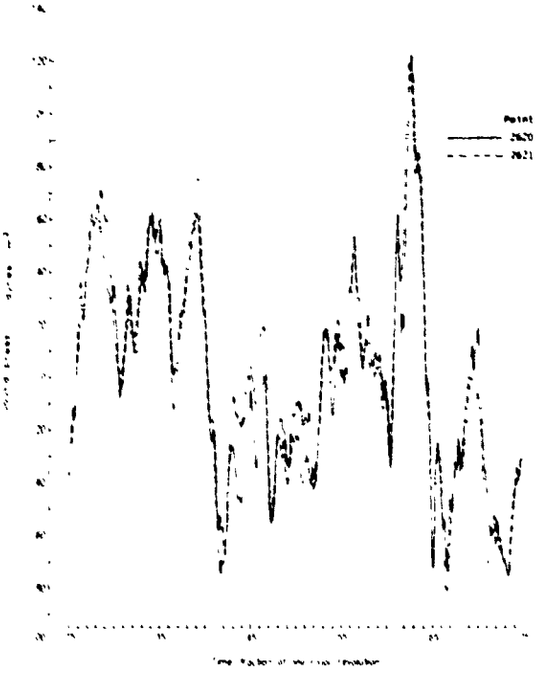

(d) Advanced rotor system; 40-revolution average from microphone 5.

Figure 7.- Concluded.

The data presented in figure 7 show comparisons that provide a high level of confidence in the overall data quality obtained during the HSI-noise portion of this wind-tunnel test.

Interpretation of Basic Data

The most direct method for comparing acoustic data is through an analysis of acoustic pressure-time histories. Such a comparison is illustrated in figure 8(a) for a forward velocity of 80 knots. In this figure, a large, negative, almost symmetrically triangular pressure pulse dominates the waveform character in the SRS data. This large, negative pressure pulse has been shown in reference 10 to be typical of HSI noise. A much narrower, smaller amplitude, positive pressure pulse precedes the large, negative pressure pulse and has been shown in reference 9 to be attributable to blade-vortex interactions. The width of this positive pressure pulse indicates that its energy content was centered around 1700 Hz (model scale), whereas the width of the large, negative pressure pulse indicates an energy content centered around 700 Hz (model scale). Since the frequency content of these pressure pulses varies as the inverse of their period (width), a narrow impulse contains more energy at higher frequencies than one which is broader; thus, a narrow impulse possesses the potential for a greater annoyance factor to the human ear. For this paper, the term "impulsiveness" is used as a measure of the width of these pressure pulses.

Important in the analysis of most noise sources is a determination of radiated energy versus frequency content. Although not the only method for analyzing impulsive-noise sources, a spectral estimation of the characteristic waveform does indicate in what frequency band the noise is predominant. For this reason, the characteristic waveform of the SRS in figure 8(a) has been transformed into the frequency domain in figure 8(b). Frequencies up to 8000 Hz are shown. Most of the energy in the large, negative pressure pulse (typical of HSI noise) is contained in the low-frequency harmonics up to approximately 1000 Hz (model scale) (ref. 8). Similarly, most of the energy from BVI noise is contained in the 1000- to 2000-Hz frequency range (model scale). In the lower frequency range, the first peak in the plotted data represents the fundamental blade-passage frequency of approximately 43.3 Hz. The following peaks represent the harmonics of the fundamental blade-passage frequency. Because this paper is concerned primarily with a comparison of high-speed impulsive noise, the lower frequency harmonics up to approximately 1000 Hz are of most concern.

Acoustical Performance

Important observations made on both the SRS and the ARS are discussed in this section. Also, important observations made on the differences between the SRS and the ARS are discussed here. The entire data set obtained from this experiment is included in the appendix.

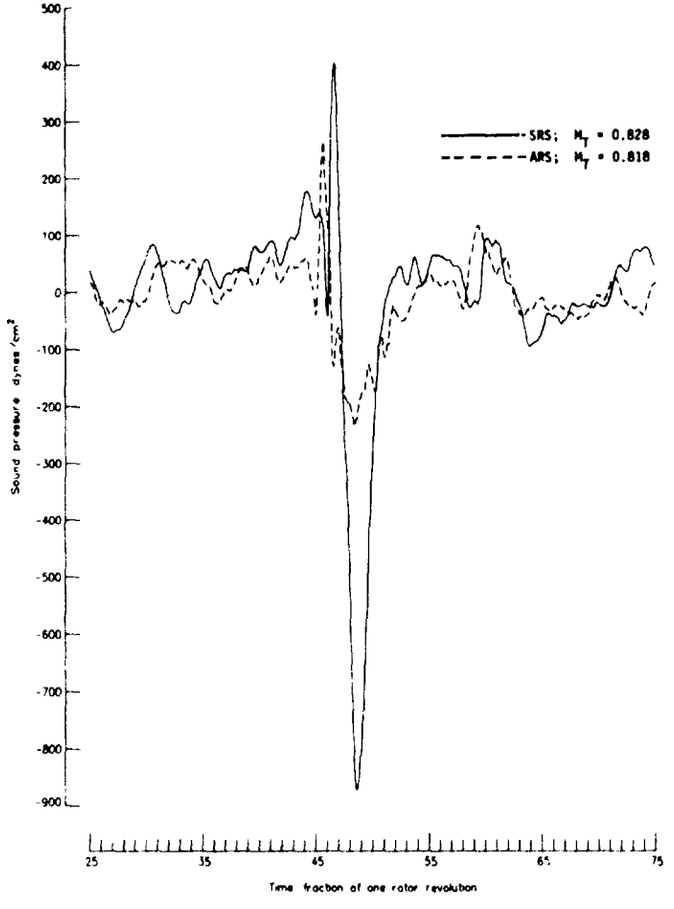

(a) Comparison of pressure-time histories for microphone 4.

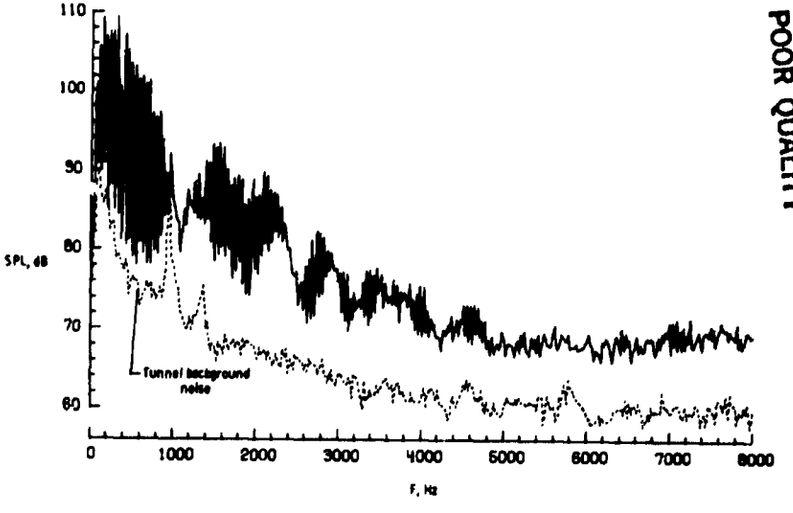

(b) Narrow-band spectrum for standard rotor system for microphone 4.

Figure 8.- Effect of rotor system on noise signature generated by helicopter model at V_∞ = 80 knots.

Analysis of the pressure-time histories from microphone 4 for the SRS shows that the amplitude of the HSI-noise pressure spike increased from 870 dynes/cm^2 at M_T = 0.828 to 1930 dynes/cm^2 at M_T = 0.866 (fig. 9). An increase in impulsiveness (decreasing pulse width) corresponding to this increase in noise-spike amplitude with increasing M_T can also be seen in figure 9. As measured at the reference pressure of 0 dynes/cm^2, this noise-spike duration encompasses about 0.00194 sec at M_T = 0.835, whereas at M_T = 0.859 the pulse decreased to a duration of about 0.00125 sec.

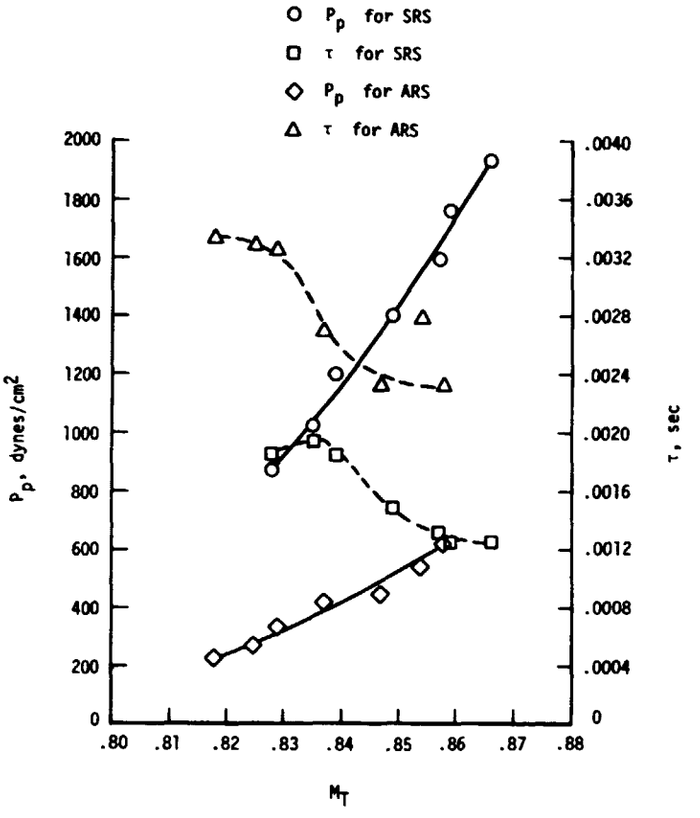

Figure 9.- Peak negative impulse pressure and reference impulse width variation as functions of advancing-blade-tip Mach number from microphone 4.

Analysis of the pressure-time histories from microphone 4 for the ARS shows that the amplitude of the HSI-noise pressure spike increased from 225 dynes/cm^2 at M_T = 0.818 to 630 dynes/cm^2 at M_T = 0.858 (fig. 9). The impulsiveness of these HSI-noise spikes follows the same trends for the ARS as was seen for the SRS. An increase in impulsiveness corresponding to this increase in noise-spike amplitude with increasing M_T can be seen for the ARS in figure 9. Again, as measured at the reference pressure of 0 dynes/cm^2, the noise-spike duration decreases from 0.00333 sec at M_T = 0.818 to 0.00230 sec at M_T = 0.858. Figure 9 also shows that, for a given forward-flight speed, the two rotor systems operated at slightly different rotor advancing-blade-tip Mach numbers, even though the rotor rpm's were identical. These M_T differences were due to changes in humidity, which affect the speed of sound.

Comparisons of the pressure-time histories obtained from microphone 4 for both the SRS and ARS show that the ARS reduced the amplitude of the HSI-noise pressure spike by 74 percent at V_∞ = 80 knots (fig. 8(a)) and by 68 percent at V_∞ = 110 knots (fig. 10).

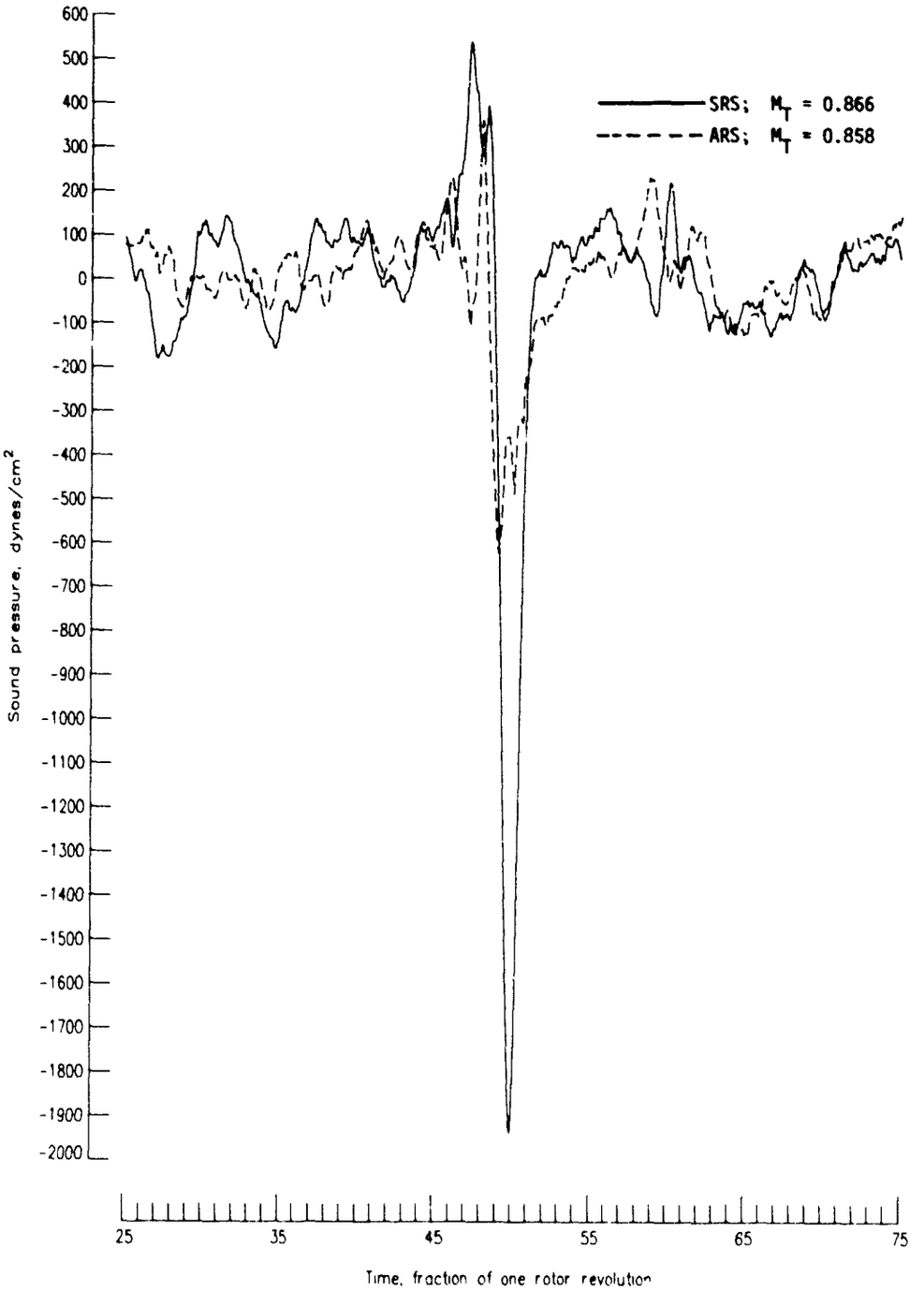

Figure 10.- Comparison of pressure-time histories for microphone 4 at V_∞ = 110 knots.

This HSI-noise spike is not only reduced in amplitude but is also less impulsive, as it has a wider waveform compared with the SRS noise spike. (See also fig. 9.) However, the contributions to HSI noise for both the SRS and the ARS are in the band of 0 to 1000 Hz for all V_∞ tested. There also appear to be more blade-vortex interactions taking place with the ARS than with the SRS, at least for a free-stream velocity of 110 knots (fig. 10).

A comparison of the narrow-band spectrum plots for the SRS and the ARS as measured at microphone 4 (see the appendix) shows a substantial decrease in sound pressure level (SPL) in the ARS data for frequencies up to 1000 Hz. At frequencies above 1000 Hz, the ARS SPL either remains unchanged or, in most cases, actually increases slightly compared with the SRS. These results can be seen clearly in figure 11, which presents the SPL difference (ΔSPL) between the SRS data and the ARS data as a function of frequency F and free-stream velocity. In this figure, a positive ΔSPL indicates that the ARS reduced the SPL, whereas a negative ΔSPL indicates that the ARS actually increased the SPL.

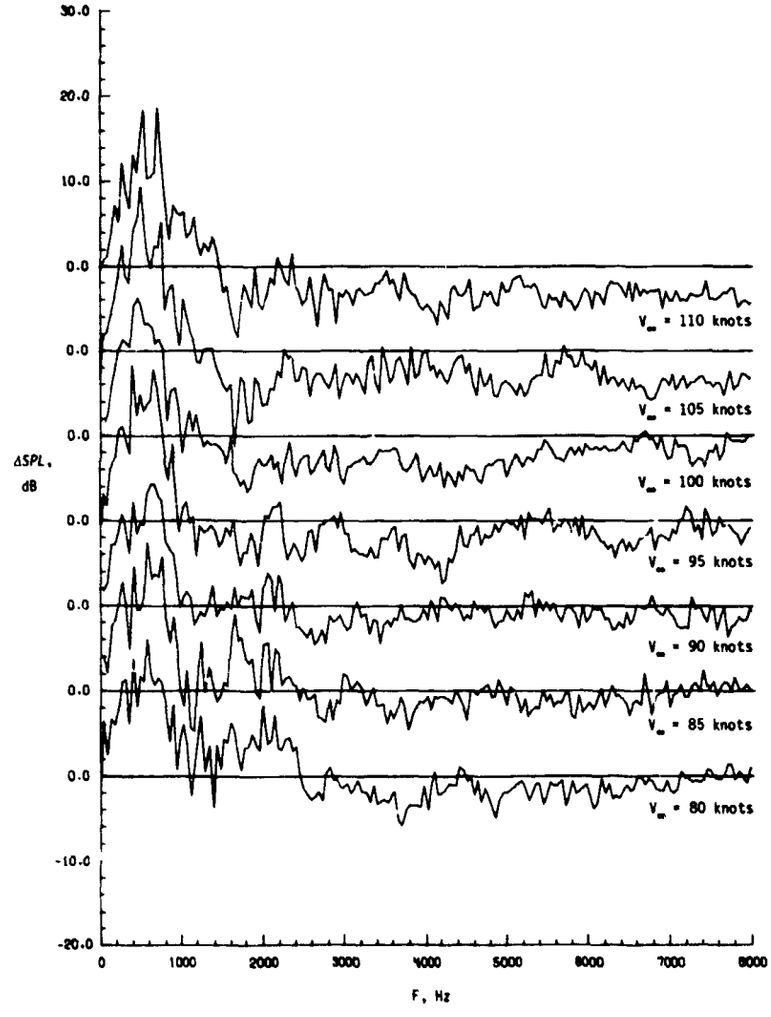

Figure 11.- Difference in sound pressure level due to advanced rotor system from microphone 4.

Figure 11 shows that for frequencies between 0 and 1000 Hz, where HSI noise is predominant, the ARS reduced the maximum SPL by 15 to 20 dB compared with the SRS. The 15-dB reduction occurred at V_∞ = 90 knots, whereas the maximum 20-dB reduction occurred at V_∞ = 105 and 110 knots. For frequencies greater than 1000 Hz, the ARS increases the SPL by an average of about 1 dB at the lower forward speeds (V_∞ = 80 to 90 knots) to an average of about 4 dB at the higher forward speeds (V_∞ = 95 to 110 knots).

Before beginning a discussion of the data collected from microphone 5, a few words about the quality of these data are appropriate. Figure 12 presents the

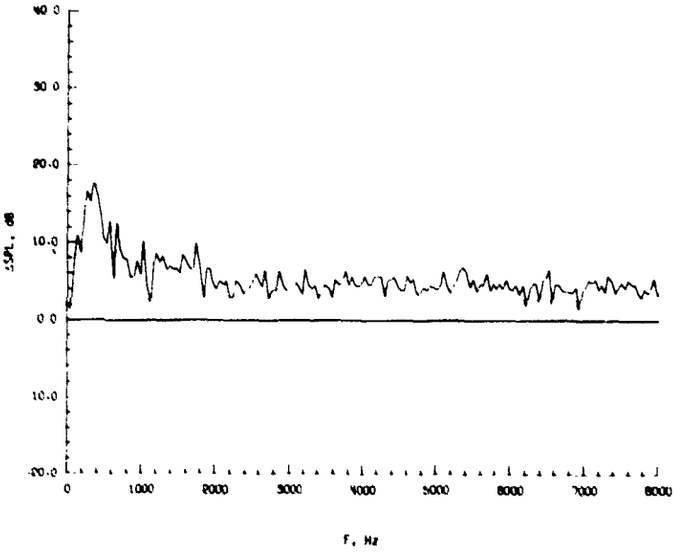

(a) Standard rotor system at V_∞ = 80 knots.

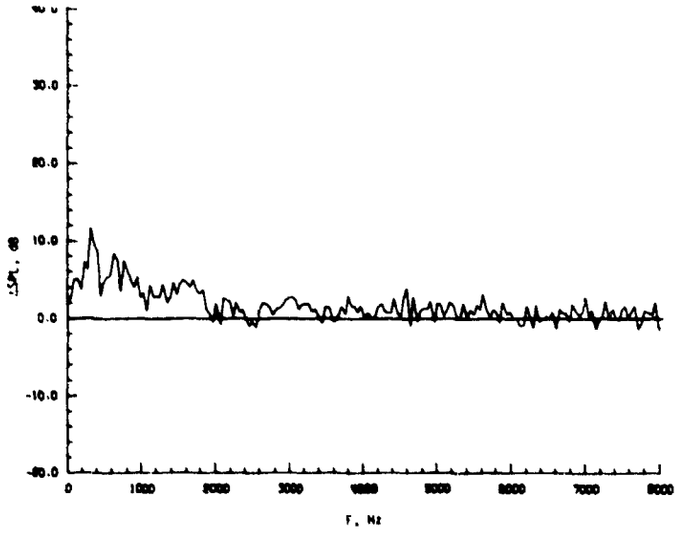

(b) Standard rotor system at V_∞ = 110 knots.

Figure 12.- Narrow-band spectrum increment above background noise from microphone 5.

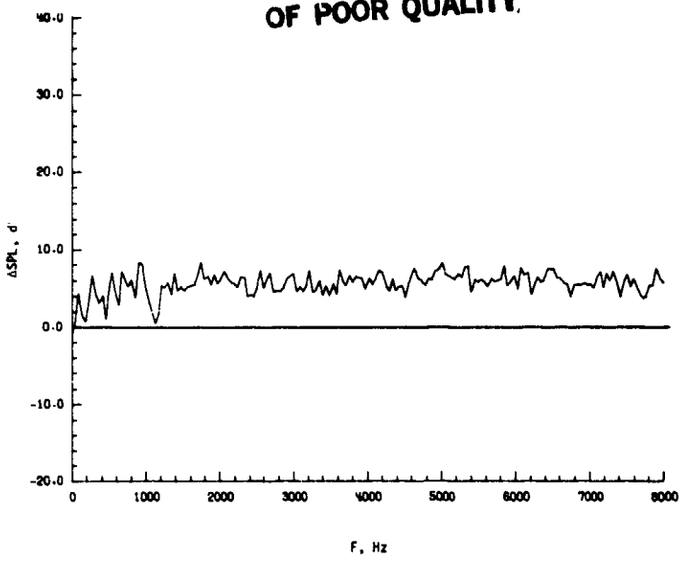

(c) Advanced rotor system at V_∞ = 80 knots.

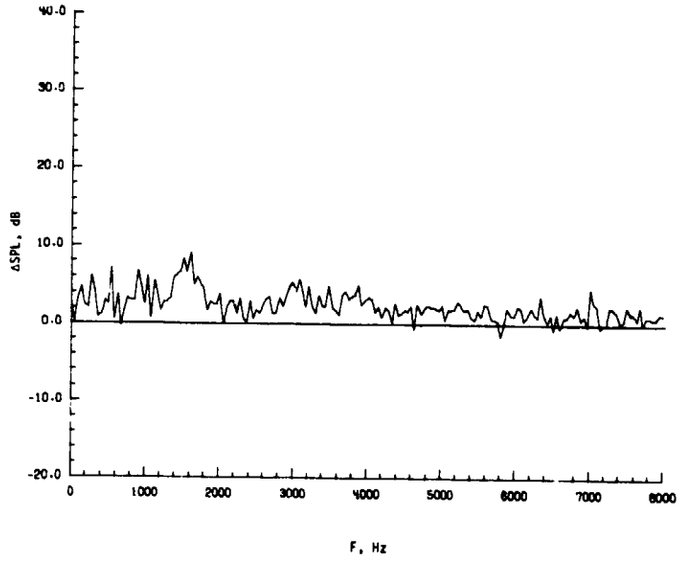

(d) Advanced rotor system at V_∞ = 110 knots.

Figure 12.- Concluded.

narrow-band spectrum increment above background noise for microphone 5 data for V_∞ = 80 and 110 knots. The vertical scale of figure 12 represents the difference in SPL between the total system noise and the background noise, with a positive ΔSPL indicating the SPL above background noise. This figure shows that for the frequency range of concern (0 to 1000 Hz), the SRS data are 6 to 18 dB above the background noise at V_∞ = 80 knots (fig. 12(a)) and 4 to 12 dB above background noise at V_∞ = 110 knots (fig. 12(b)). These levels are sufficiently above background-noise levels to consider the SRS data not contaminated by background noise. In contrast to the SRS data, the ARS data at V_∞ = 80 knots (fig. 12(c)) and at V_∞ = 110 knots (fig. 12(d)) are only 2 to 5 dB above the background noise at frequencies of 0 to

1000 Hz, thus leaving doubt as to the validity of these ARS data. Nevertheless, figure 12 shows that while the SRS data are well above the background-noise levels between 0 and 1000 Hz, the ARS is so quiet that its noise data are down near the levels of the background noise.

Analysis of the pressure-time histories from microphone 5 for the SRS shows that the amplitude of the HSI-noise pressure spike increased from a minimum of 360 dynes/cm^2 at V_∞ = 80 knots (fig. 13(a)) to a maximum of 420 dynes/cm^2 at V_∞ = 100 knots (fig. 13(b)). The impulsiveness of this spike also changed very little with increasing free-stream velocity, indicating that neither the amplitude nor the impulsiveness of this spike is a function of forward speed (as measured in this microphone position). The duration of this HSI-noise spike is approximately 0.0022 sec throughout the M_T range compared with 0.00185 sec at M_T = 0.828 and 0.00125 sec at M_T = 0.866 for microphone 4 data (fig. 9). In addition, there appears to be no distinct BVI noise present in these data as there was in the data of microphone 4.

Analysis of the pressure-time histories from microphone 5 for the A [illegible] ig. 13) reveals that no HSI-noise spikes or BVI-noise spikes appear anywhere in these data at any forward speed. The pressure-amplitude range of these data is small and rarely exceeds ±100 dynes/cm^2, indicating that there is relatively little energy content.

A comparison of the narrow-band spectrum plots for the SRS and the ARS as measured at microphone 5 (see the appendix and fig. 14 for increment presentation) shows a substantial SPL decrease in the ARS data at the lower frequencies, whereas the SPL is unchanged or increases at the higher frequencies. Between 0 and 1000 Hz, which is the range in which HSI noise is predominant, a decrease in SPL of as much as 15 dB is seen with the ARS at the lower free-stream velocity of 80 knots, whereas at the highest free-stream velocity of 110 knots, this SPL decrease is reduced to a maximum of 9 dB. This decrease in SPL reduction with increasing free-stream velocity is not due to an increase in the ARS SPL or a decrease in the SRS SPL; it is due to tunnel background-noise contamination of the ARS data. At the lowest free-stream velocity of 80 knots, figure 12(c) shows that the tunnel background noise is contaminating the ARS data at the lower frequencies, whereas figures 12(b) and 12(d) show that at V_∞ = 110 knots both the SRS and the ARS data are totally contaminated at all frequencies. This contamination by background noise does not exist for the data obtained with microphone 4, except at one or two discrete frequencies at V_∞ = 80 knots. (See the appendix.)

Figure 15 shows a comparison of the overall sound pressure level (OASPL) in decibels for the SRS and the ARS as a function of advancing-blade-tip Mach number. The OASPL is used here because it gives a strong indication of the energy content of the lower frequencies, which is the area of concern of this paper. Also plotted in figure 15 is the OASPL for frequencies up to 1000 Hz only. If the HSI noise is strong, these two curves should fall nearly on top of each other. As the HSI noise decreases, the OASPL curve for 0 to 1000 Hz should tend to drop below the OASPL curve for all frequencies. This figure shows that for the SRS, which has a strong HSI-noise content, the two OASPL curves fall nearly on top of each other. For the ARS, however, which has less HSI noise, the OASPL curve for 0 to 1000 Hz does tend to drop slightly below the OASPL curve for all frequencies at all advancing-blade-tip Mach numbers. In figure 15(a) (microphone 4), the OASPL for the ARS has been reduced by 7 dB at the lower blade-tip Mach numbers and by 5 dB at the higher blade-tip Mach numbers. In fact, the ARS generates less noise at 110 knots (M_T = 0.858) than the SRS at 80 knots (M_T = 0.828). The tunnel background noise is also shown in figure 15(a) and is 8 to 10 dB lower than the ARS data. It appears the tunnel

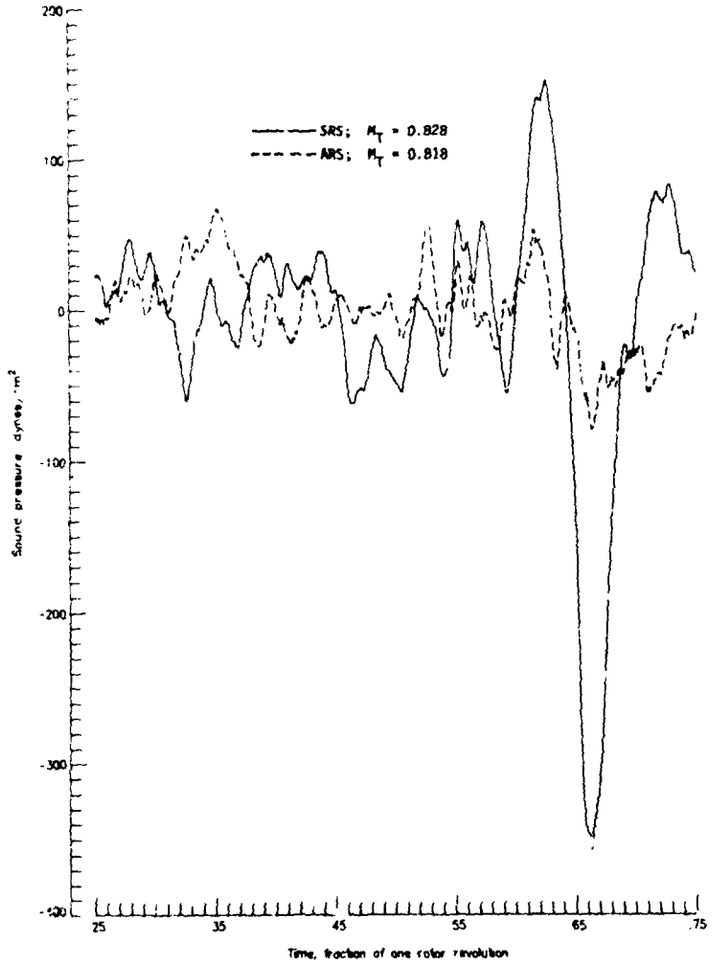

(a) V_∞ = 80 knots.

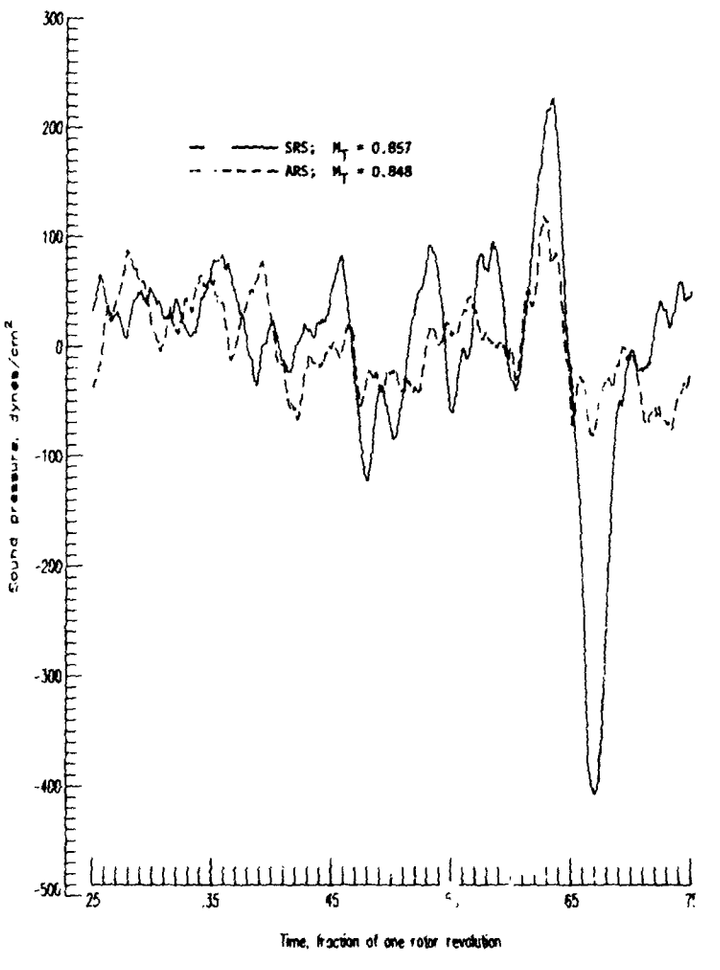

(b) V_∞ = 100 knots.

Figure 13.- Comparison of pressure-time histories for microphone 5.

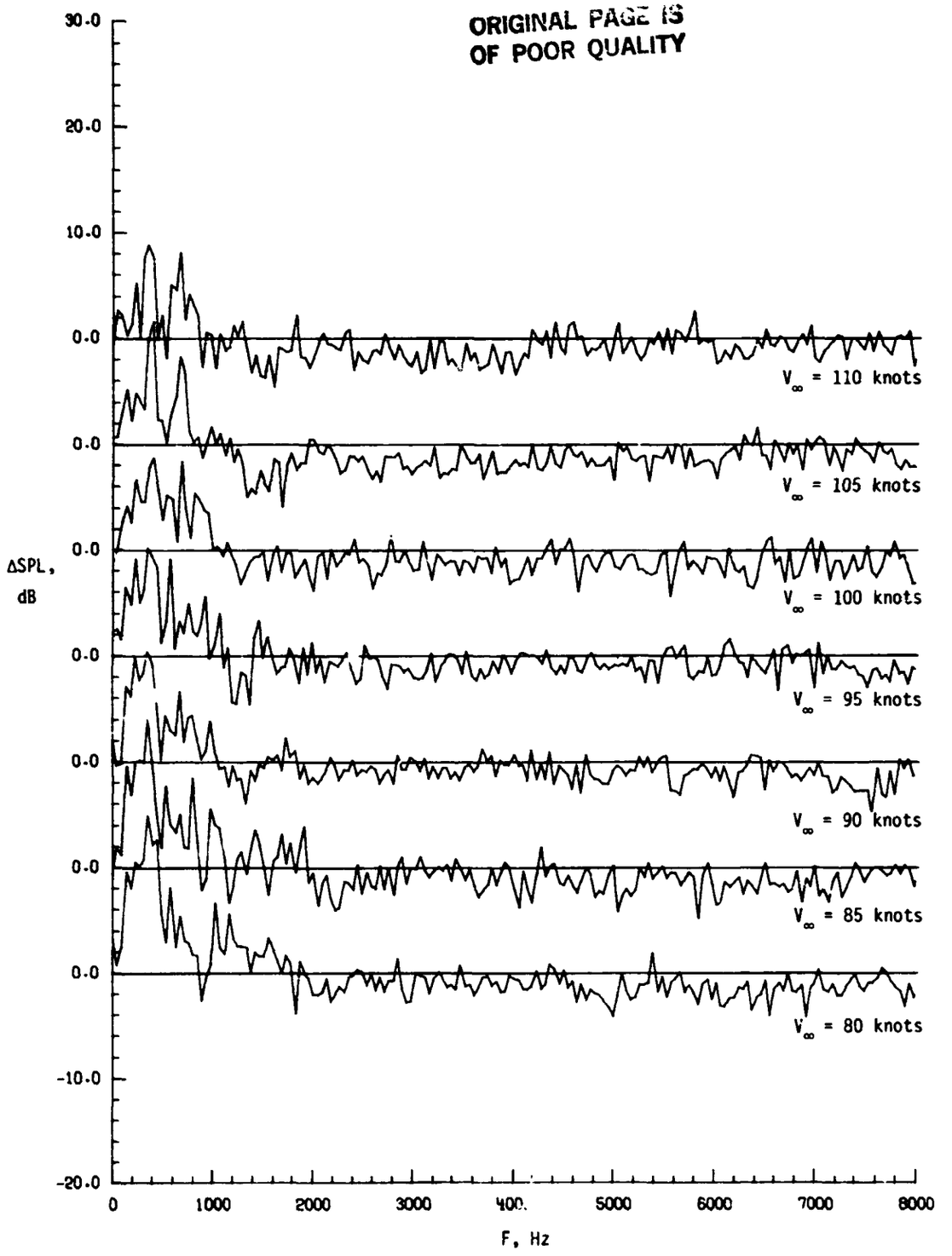

Figure 14.- Difference in sound pressu[illegible] advanced rotor system from micro[illegible]

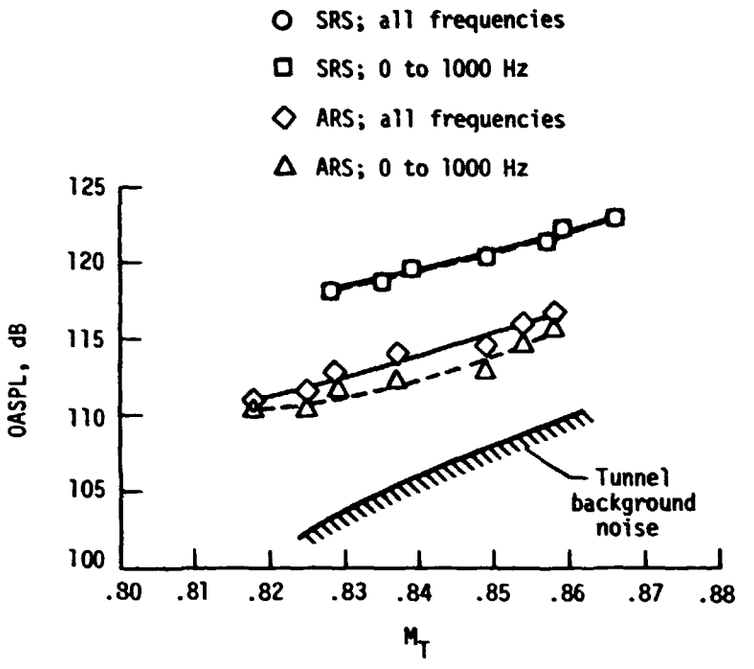

(a) Microphone 4.

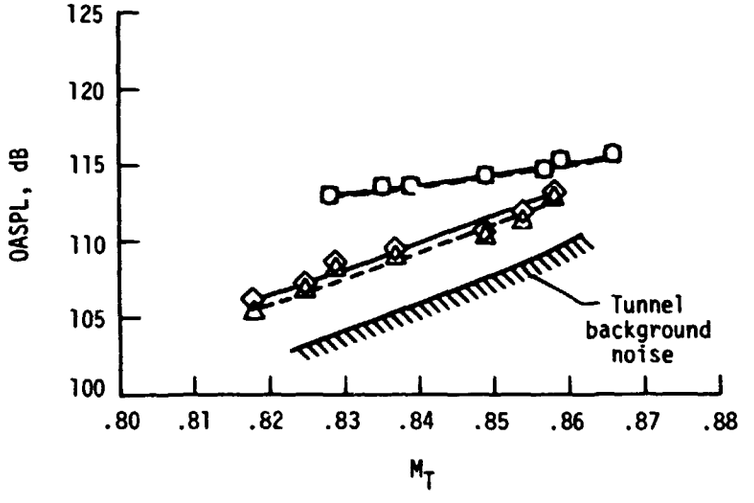

(b) Microphone 5.

Figure 15.- Overall sound pressure level generated by standard and advanced rotor systems.

background noise could possibly be pushing up the value of the ARS OASPL at the higher blade-tip Mach numbers. Figure 15(b) shows a plot of the OASPL in decibels for microphone 5 as a function of the advancing-blade-tip Mach number. This plot shows the ARS OASPL to be reduced by 6 dB at the lower Mach numbers and by only 2 dB at the higher Mach numbers compared with the SRS data.

CONCLUSIONS

An experimental investigation was conducted in the Langley 4- by 7-Meter Tunnel to determine the high-speed impulsive-noise characteristics of a new advanced main rotor system for the UH-1H helicopter. A 1/4-scale model of the UH-1H fuselage was fitted to the general rotor model system (GRMS) of the Langley Research Center. Two different dynamically scaled rotor systems were tested, each mounted on the same geometrically scaled version of the UH-1H helicopter hub. The first rotor system tested used the standard, or baseline, rotor blades which were geometrically and dynamically scaled to the current UH-1H rotor blades. An advanced set of rotor blades with higher twist, advanced airfoil sections, considerable taper, and dynamic characteristics similar to the standard system was also tested. Acoustic data were taken with upstream microphones located in the rotor tip-path plane.

The results of this investigation can be summarized as follows:

1. The experimental procedures and data reduction methods used in the present investigation yield highly repeatable acoustic data.

2. Over the operating range investigated, the dominant high-speed impulsive-noise component was reduced by as much as 20 dB by the advanced rotor system. The maximum overall noise reduction was 6 dB.

3. The peak negative impulsive pressure was reduced by as much as 74 percent by the advanced rotor system.

4. Based on measurements made upstream of the advancing rotor blade, the overall noise generated by the advanced rotor system at 110 knots was less than that generated by the standard rotor system at 80 knots.

5. Data for the advanced rotor system from the microphone upstream of the retreating rotor blade contained no distinct high-speed impulsive-noise waveforms of any kind at any forward speed. The high-speed impulsive noise measured at this microphone for the standard rotor system showed a much weaker dependence on forward speed compared with the measurement made upstream of the advancing rotor blade.

Langley Research Center
National Aeronautics and Space Administration
Hampton, VA 23665
November 3, 1982

APPENDIX

COMPLETE HSI-NOISE ACOUSTIC DATA SET

All pressure-time history data contained herein incorporate similar plotting formats. The vertical axis presents the acoustic pressure amplitude with an absolute scale measured in dynes per centimeter squared. For resolution purposes, the vertical-scale factor varies with forward velocity. The horizontal axis preser s time and is shown as a fraction of one rotor revolution; only one-half of one rotor revolution is shown. For ease of comparison, SRS and ARS noise data are plotted on top of each other, with a solid line representing the SRS data and a dashed line representing the ARS data.

Spectral analyses of the data from the pressure-time histories are presented as narrow-band frequency plots. All narrow-band plots have identical plotting formats. The vertical axis presents the sound pressure level (SPL) in decibels. The horizontal axis presents the frequency F in hertz from 0 to 8000 Hz. For clarity, SRS and ARS spectral characteristics are plotted separately. Spectral characteristics of the tunnel background noise are also presented for maximum and minimum forward velocity only.

The complete data set obtained during the high-speed impulsive-noise portion of this investigation is presented as follows:

APPENDIX

APPENDIX

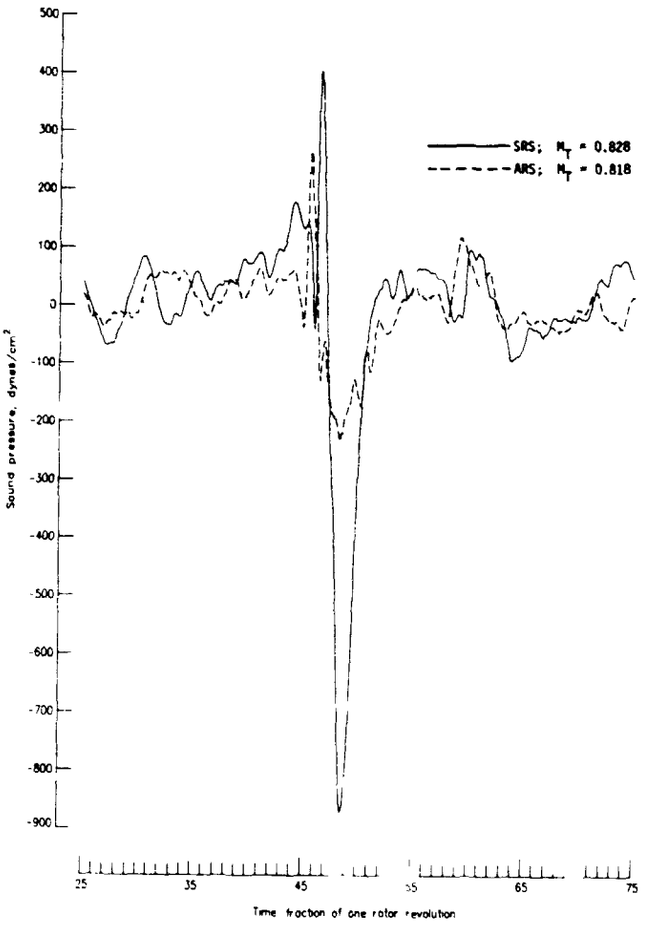

(a) Comparison of pressure-time histories for microphone 4.

Figure A1.- Effect of rotor system on noise signature generated by helicopter model at V_∞ = 80 knots.

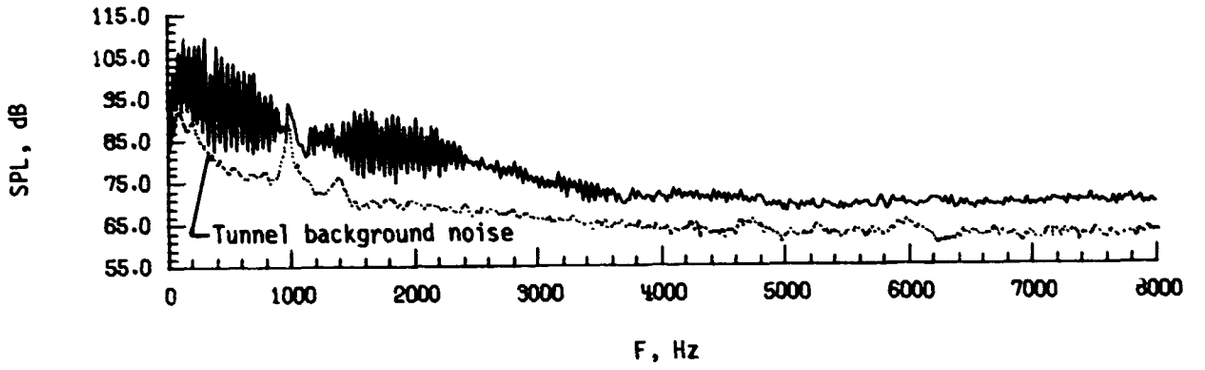

(b) Narrow-band spectrum for standard rotor system for microphone 4.

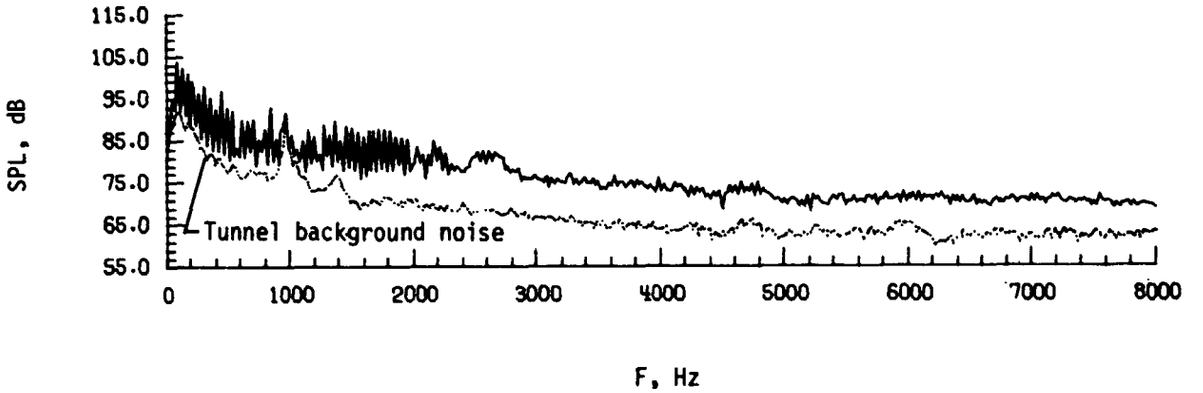

(c) Narrow-band spectrum for advanced rotor system for microphone 4.

Figure A1.- Continued.

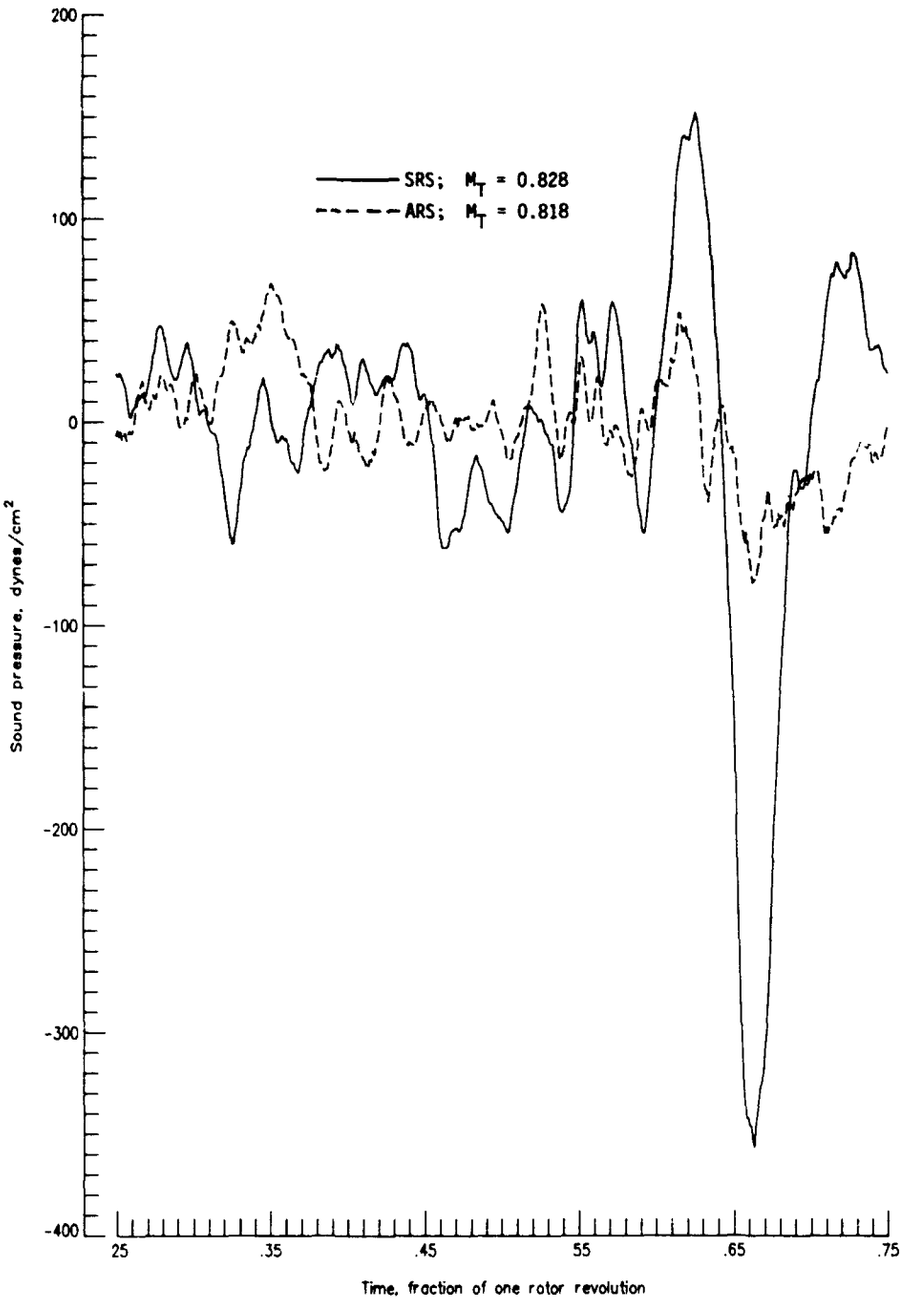

(d) Comparison of pressure-time histories for microphone 5.

Figure A1.- Continued.

APPENDIX

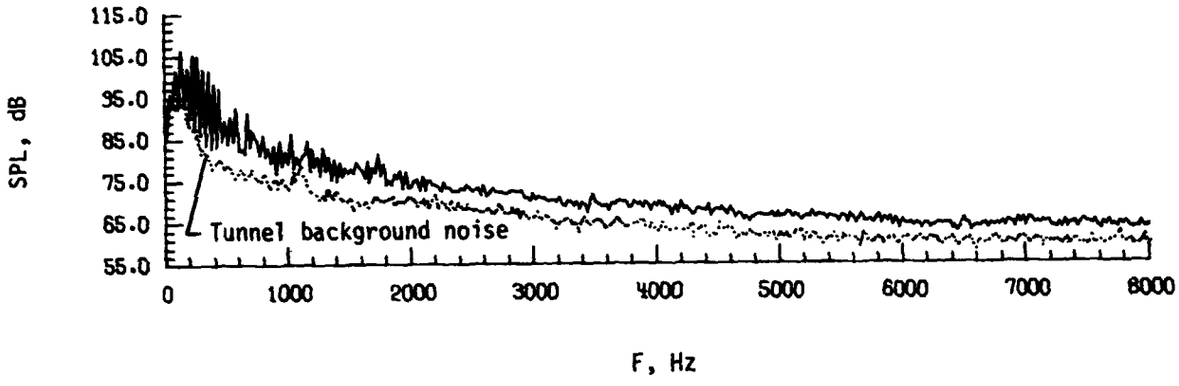

(e) Narrow-band spectrum for standard rotor system for microphone 5.

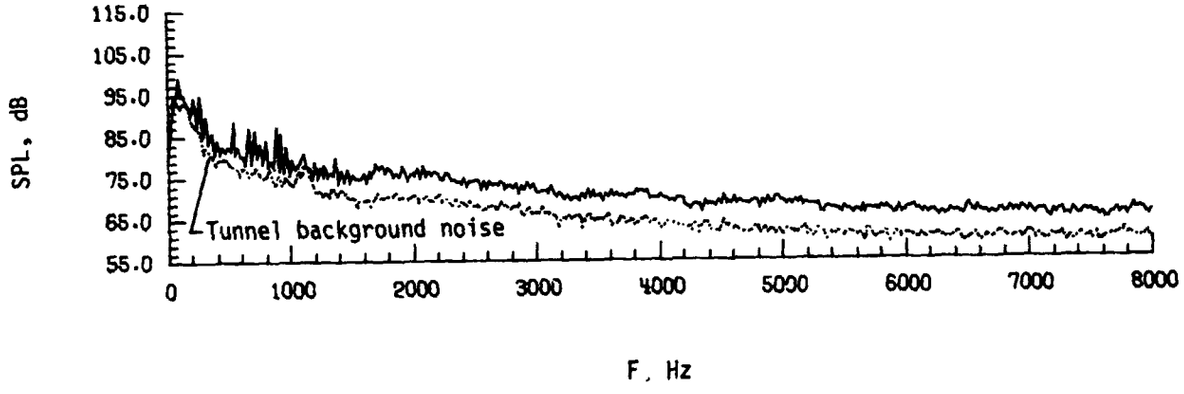

(f) Narrow-band spectrum for advanced rotor system for microphone 5.

Figure A1.- Concluded.

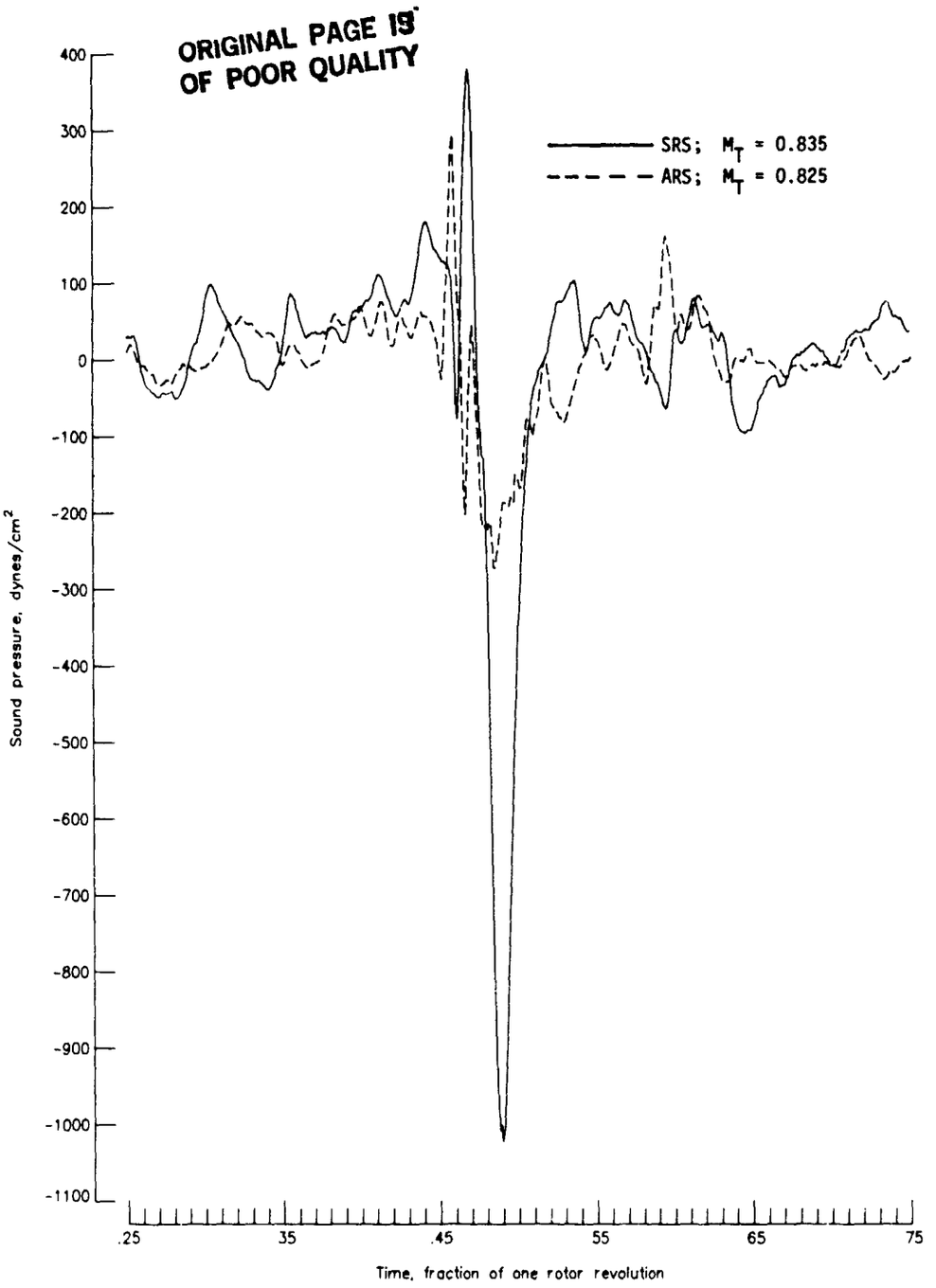

(a) Comparison of pressure-time histories for microphone 4.

Figure A2.- Effect of rotor system on noise signature generated by helicopter model at V_∞ = 85 knots.

ORIGINAL PAGE IS
OF POOR QUALITY

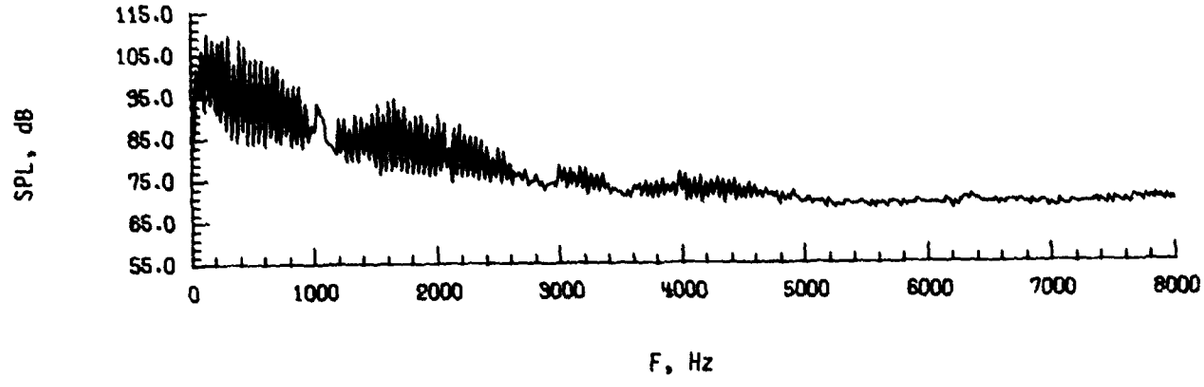

(b) Narrow-band spectrum for standard rotor system for microphone 4.

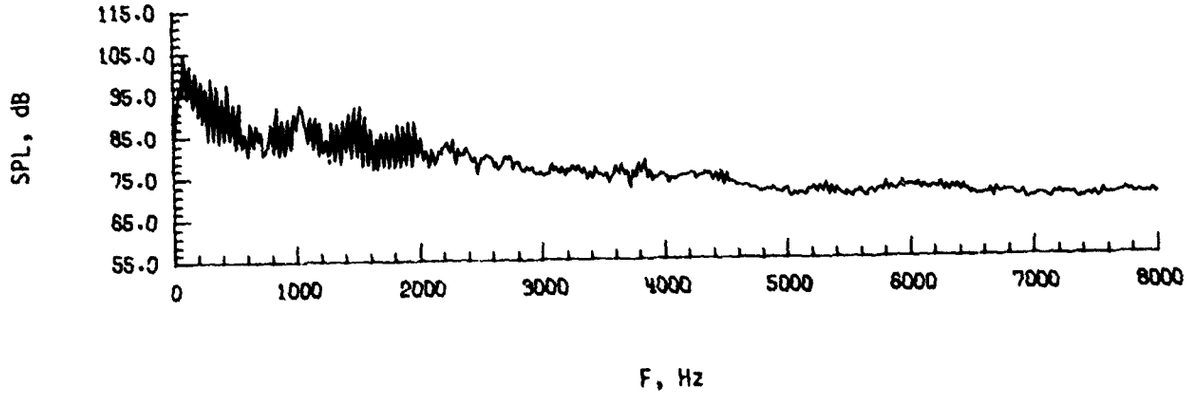

(c) Narrow-band spectrum for advanced rotor system for microphone 4.

Figure A2.- Continued.

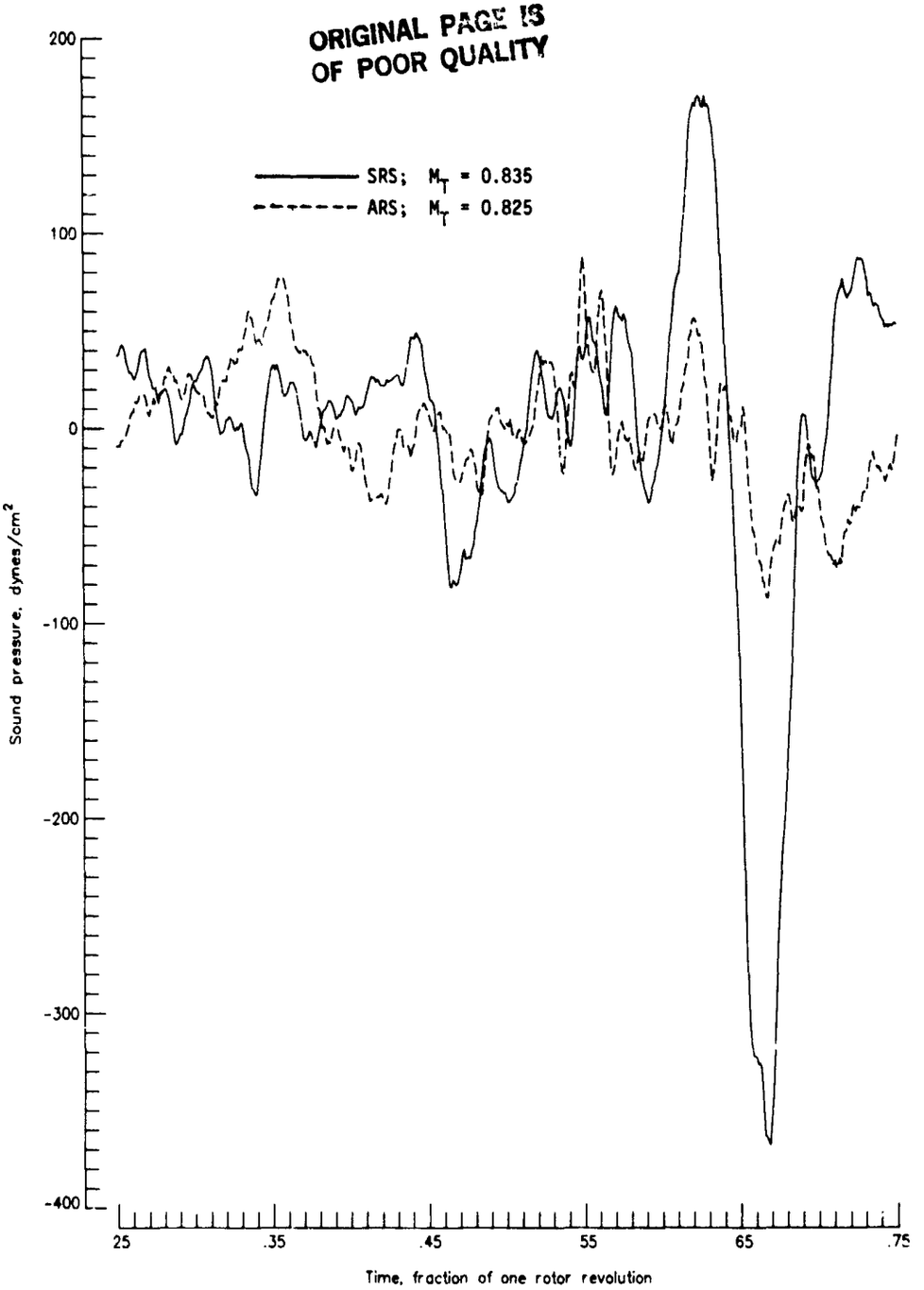

(d) Comparison of pressure-time histories for microphone 5.

Figure A2.- Continued.

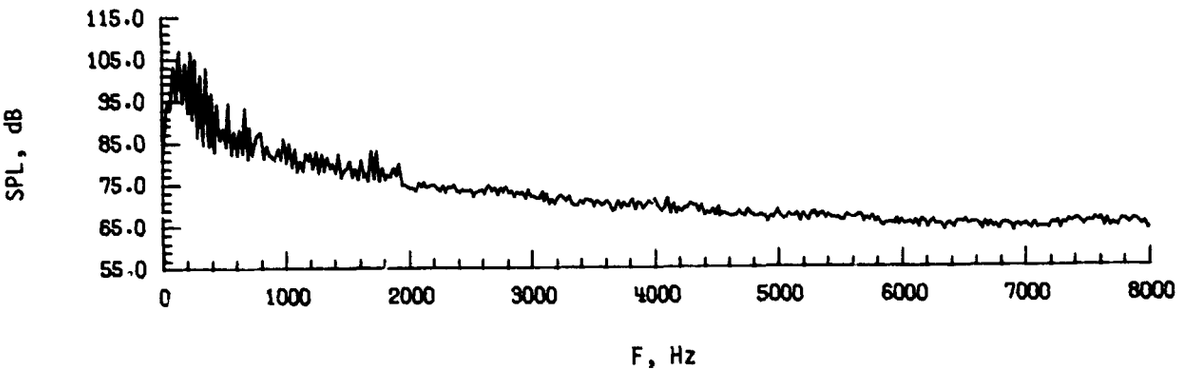

(e) Narrow-band spectrum for standard rotor system microphone 5.

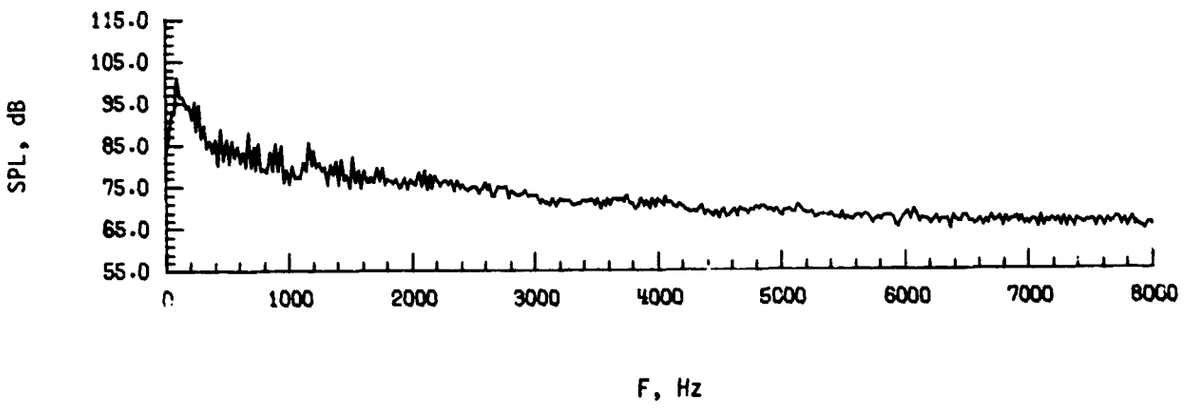

(f) Narrow-band spectrum for advanced rotor system for microphone 5.

Figure A2.- Concluded.

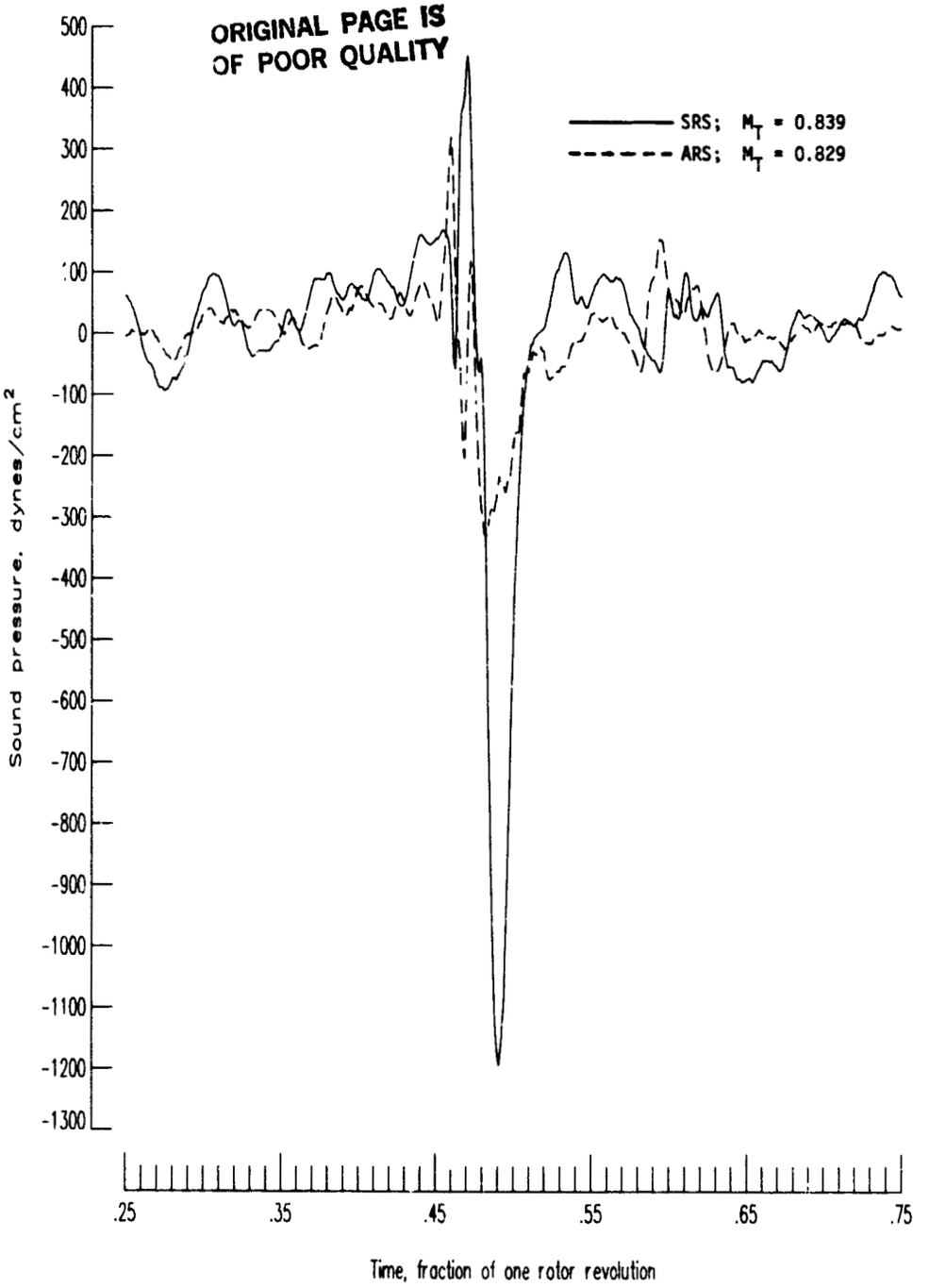

(a) Comparison of pressure-time histories for microphone 4.

Figure A3.- Effect of rotor system on noise signature generated by helicopter model at V_∞ = 90 knots.

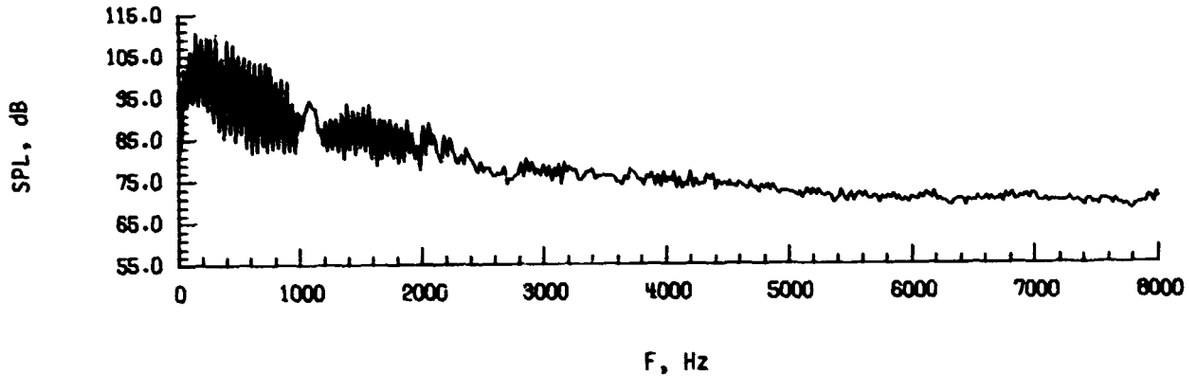

(b) Narrow-band spectrum for standard rotor system for microphone 4.

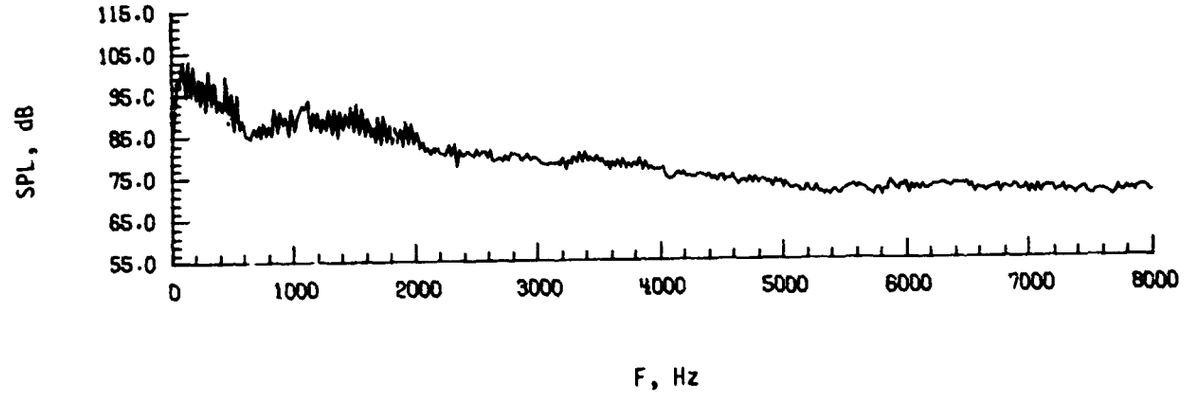

(c) Narrow-band spectrum for advanced rotor system microphone 4.

Figure A3.- Continued.

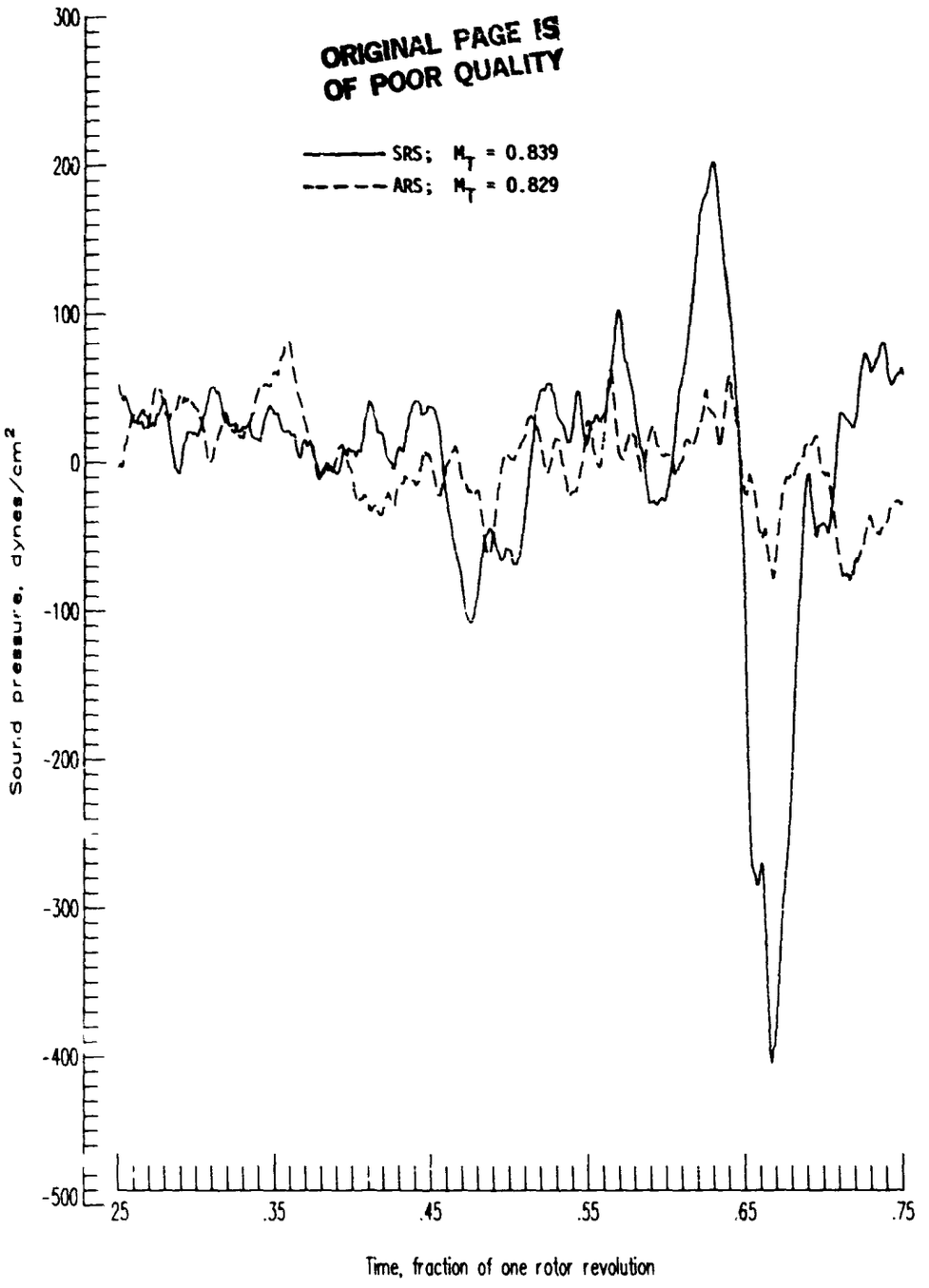

(d) Comparison of pressure-time histories for microphone 5.

Figure A3.- Continued.

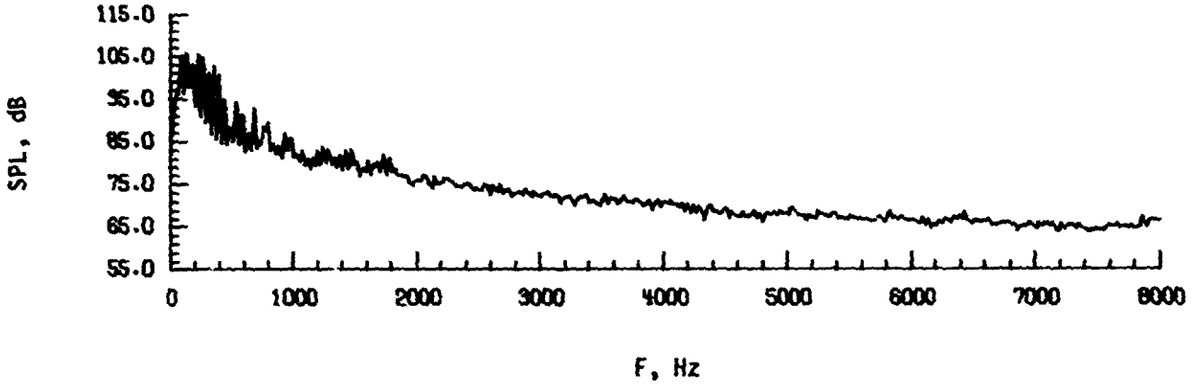

(e) Narrow-band spectrum for standard rotor system for microphone 5.

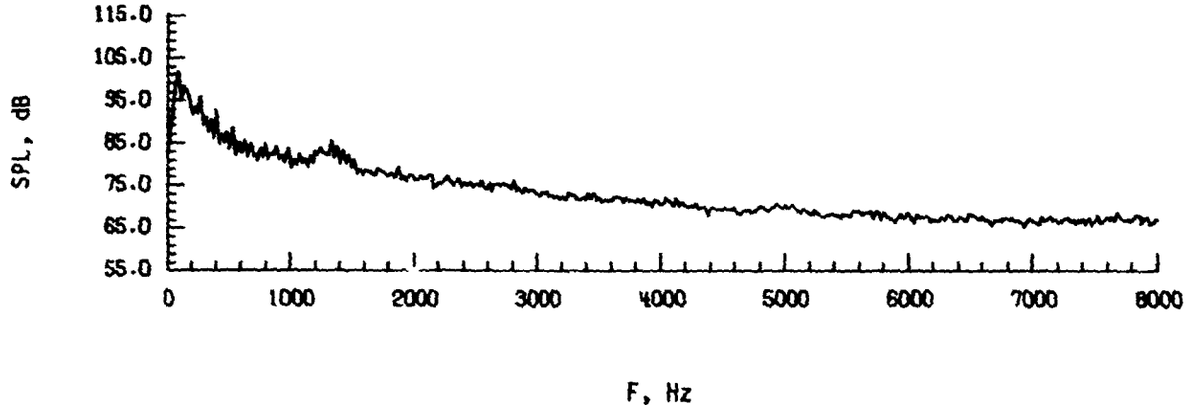

(f) Narrow-band spectrum for advanced rotor system for microphone 5.

Figure A3.- Concluded.

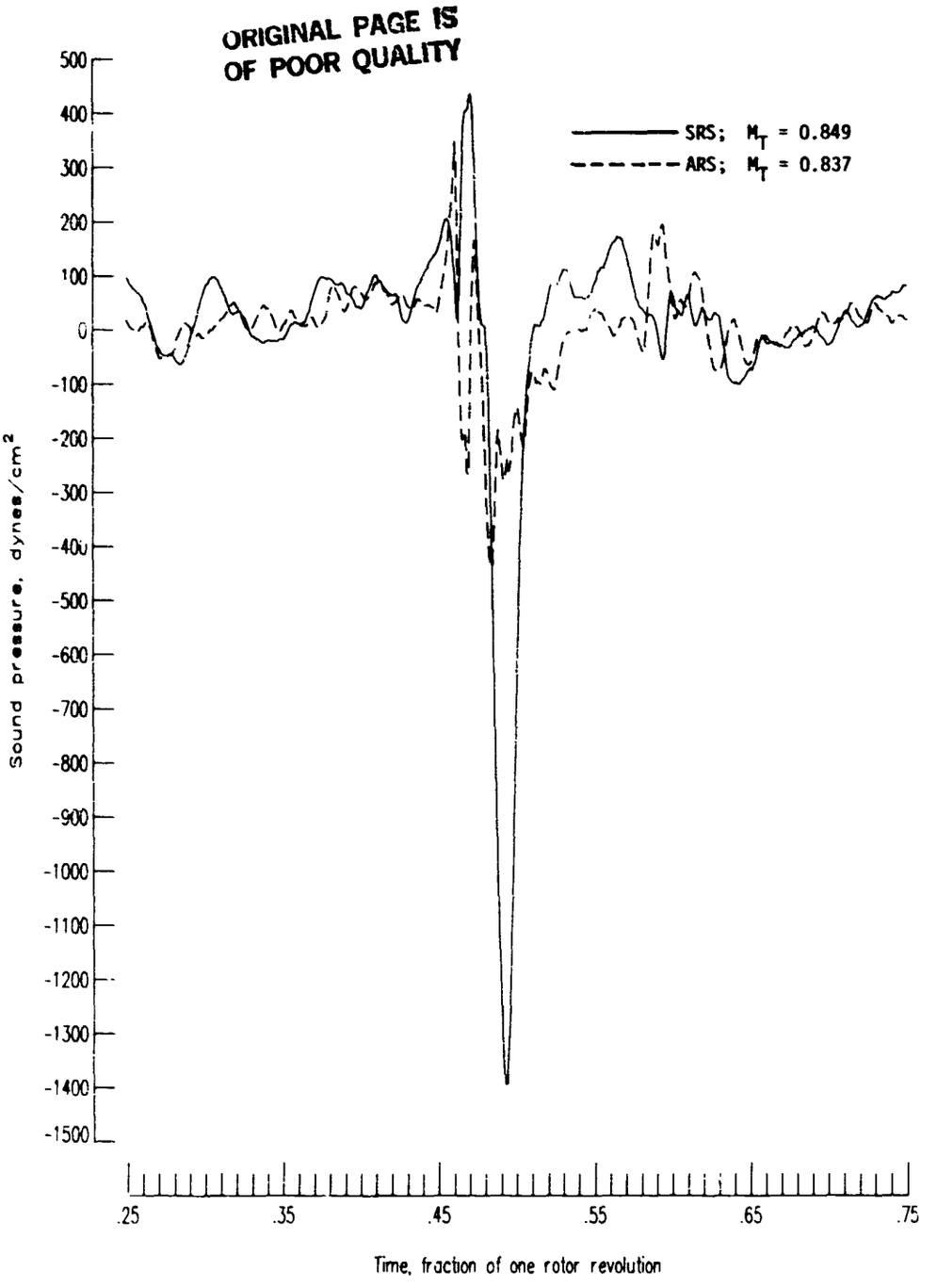

(a) Comparison of pressure-time histories for microphone 4.

Figure A4.- Effect of rotor system on noise signature generated by helicopter model at V_∞ = 95 knots.

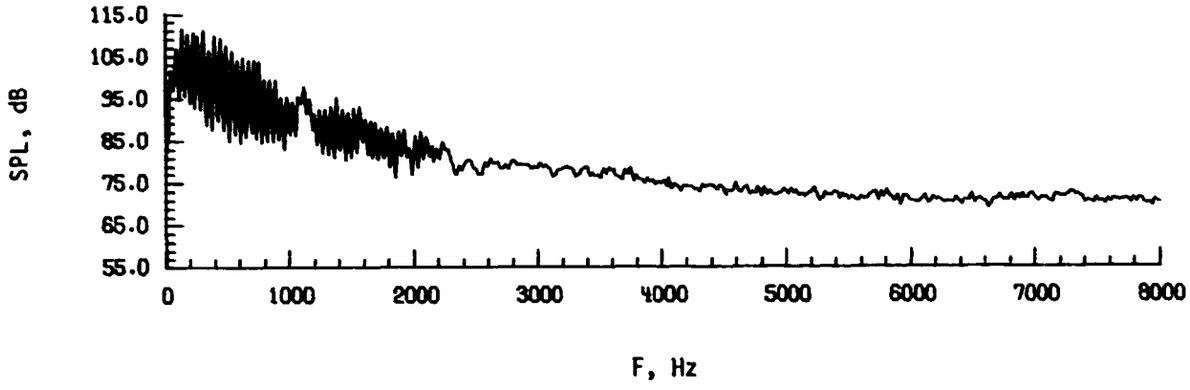

(b) Narrow-band spectrum for standard rotor system for microphone 4.

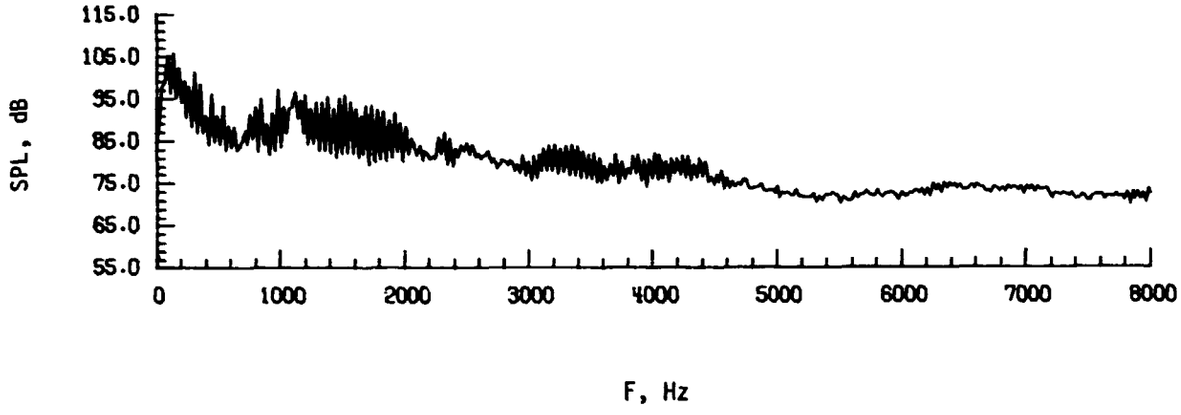

(c) Narrow-band spectrum for advanced rotor system for microphone 4.

Figure A4.- Continued.

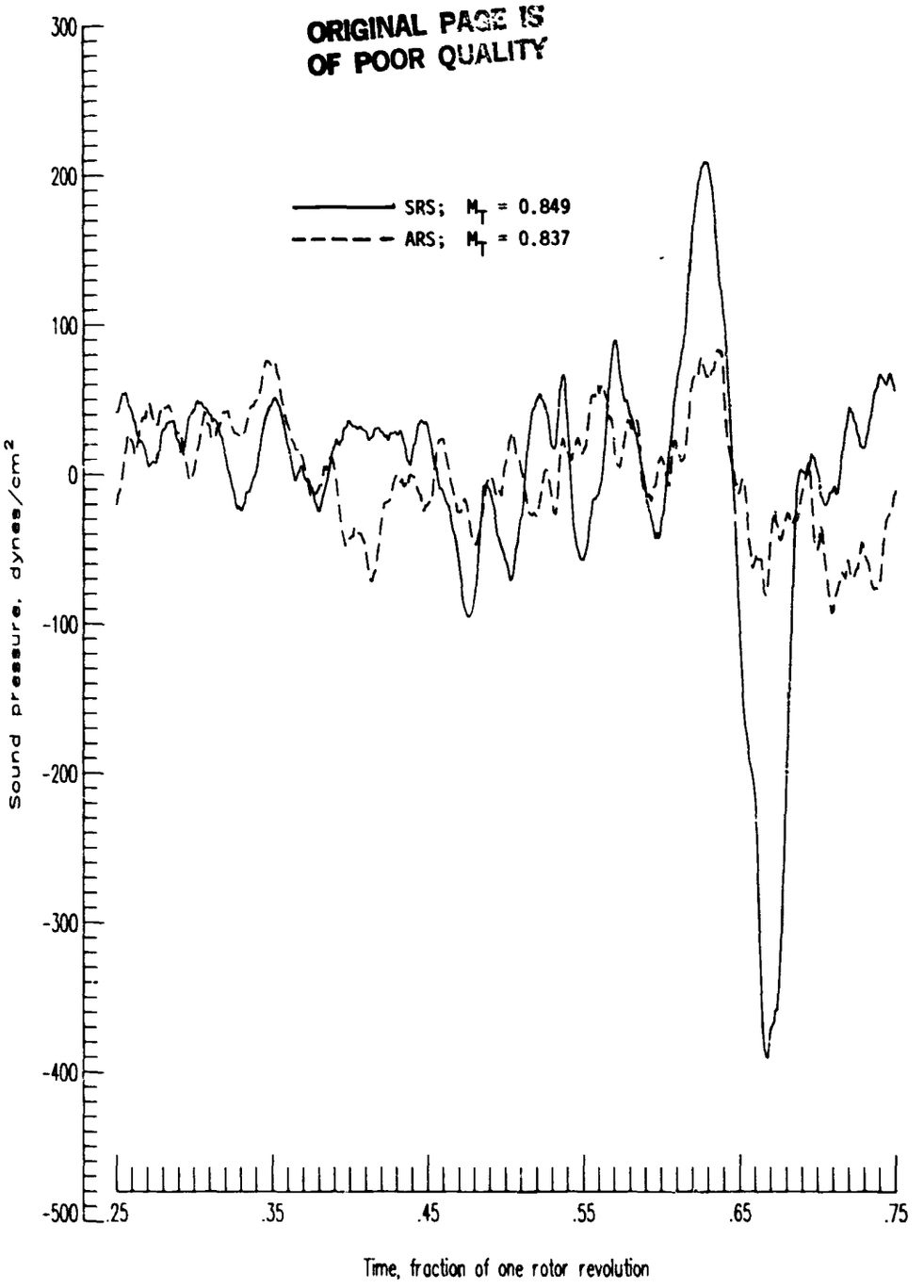

(d) Comparison of pressure-time histories for microphone 5.

Figure A4.- Continued.

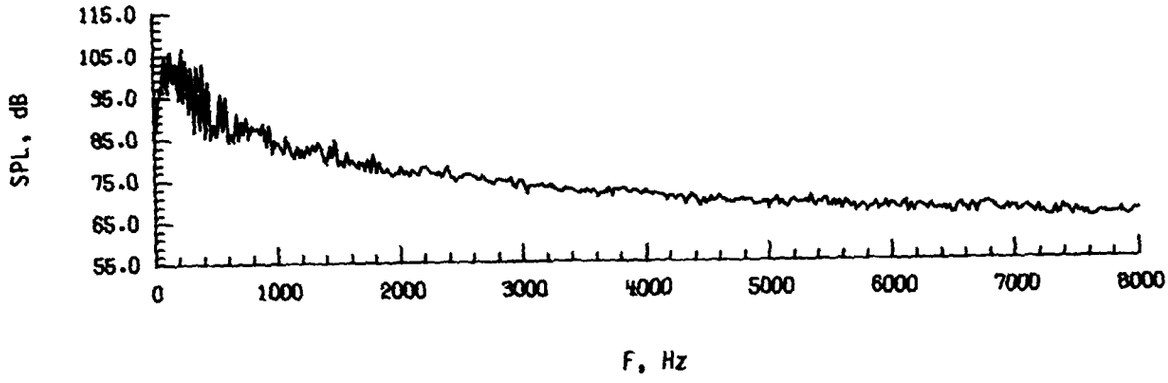

(e) Narrow-band spectrum for standard rotor system for microphone 5.

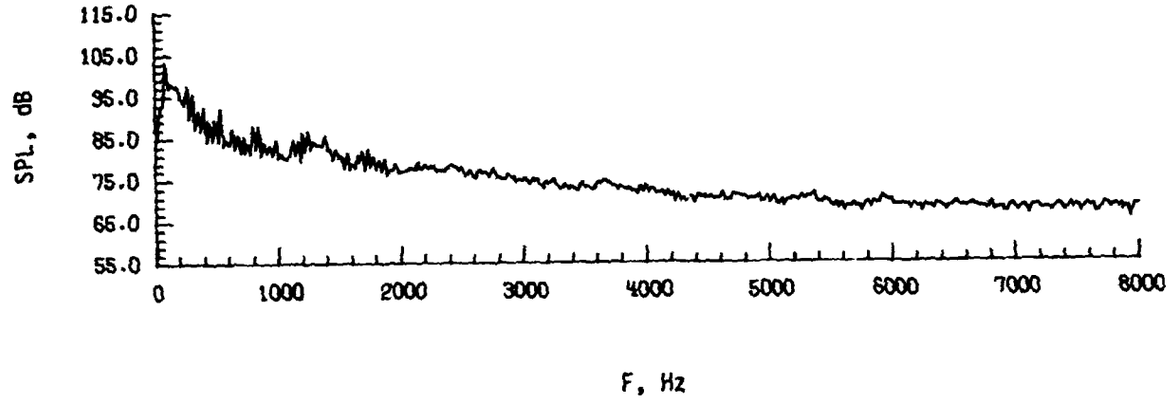

(f) Narrow-band spectrum for advanced rotor system for microphone 5.

Figure A4.- Concluded.

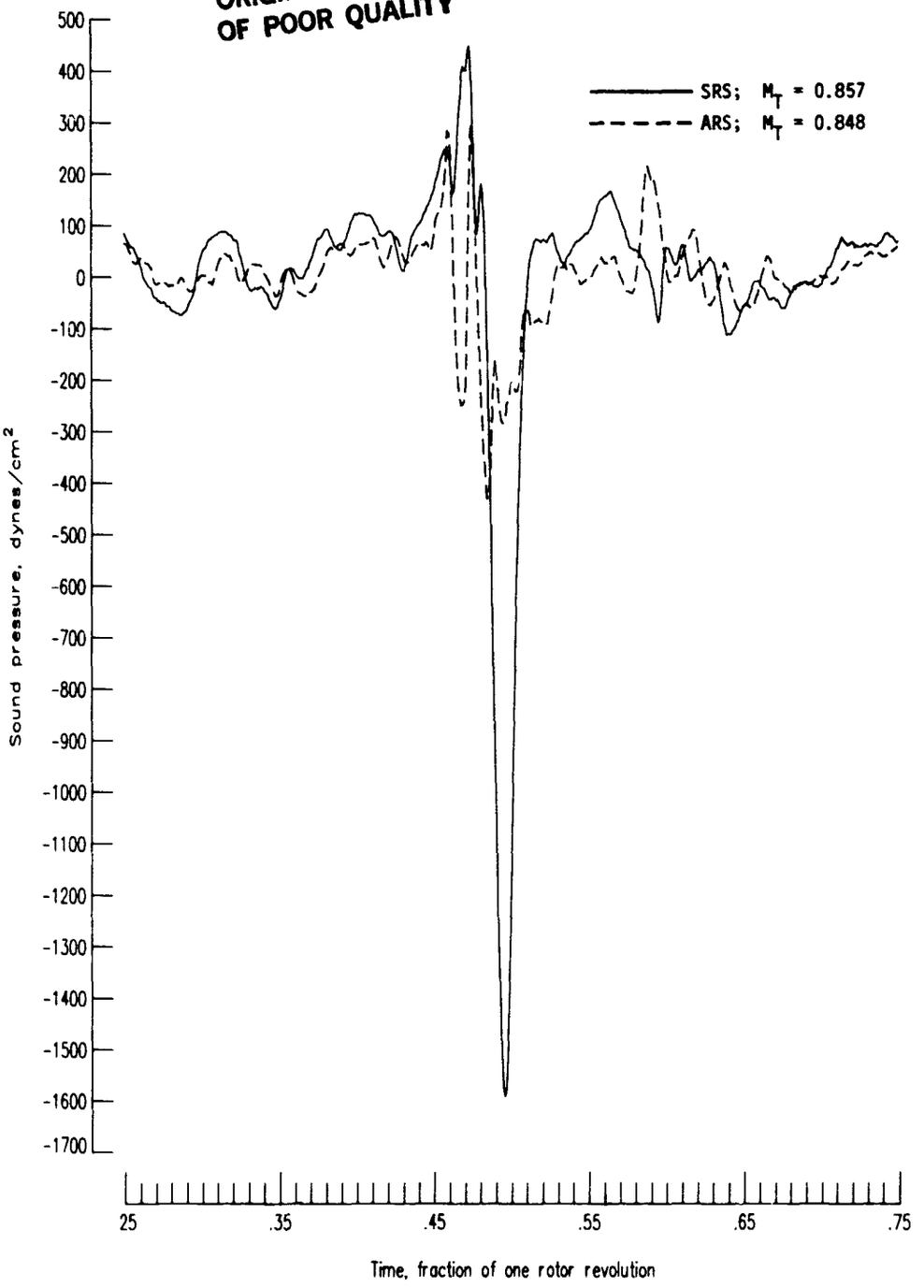

(a) Comparison of pressure-time histories for microphone 4.

Figure A5.- Effect of rotor system on noise signature generated by helicopter model at V_∞ = 100 knots.

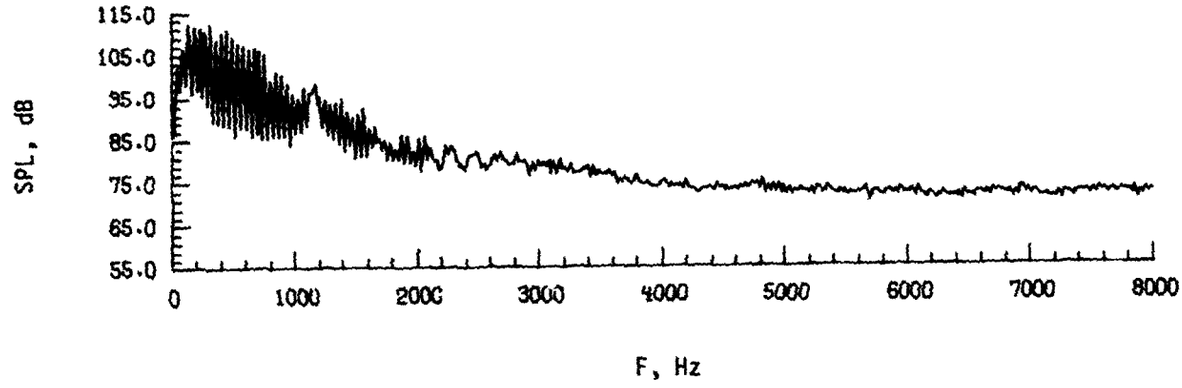

(b) Narrow-band spectrum for standard rotor system for microphone 4.

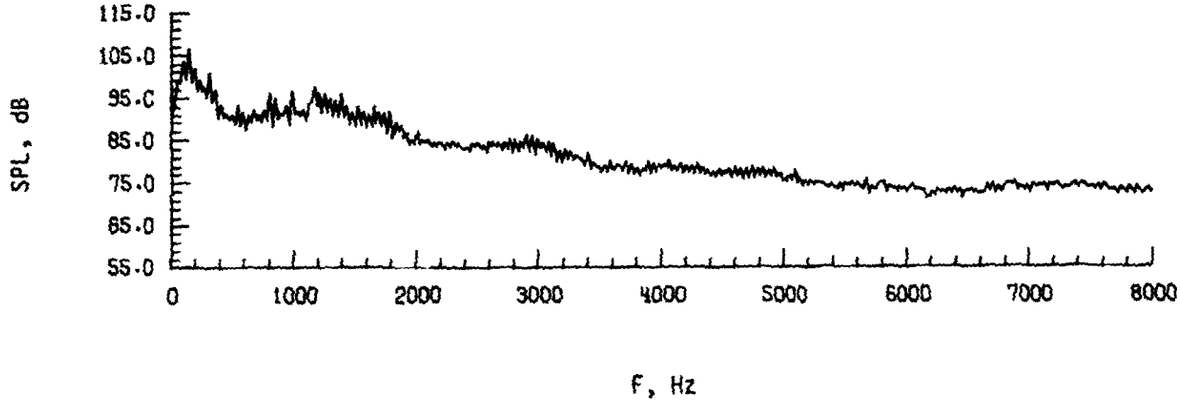

(c) Narrow-band spectrum for advanced rotor system for microphone 4.

Figure A5.- Continued.

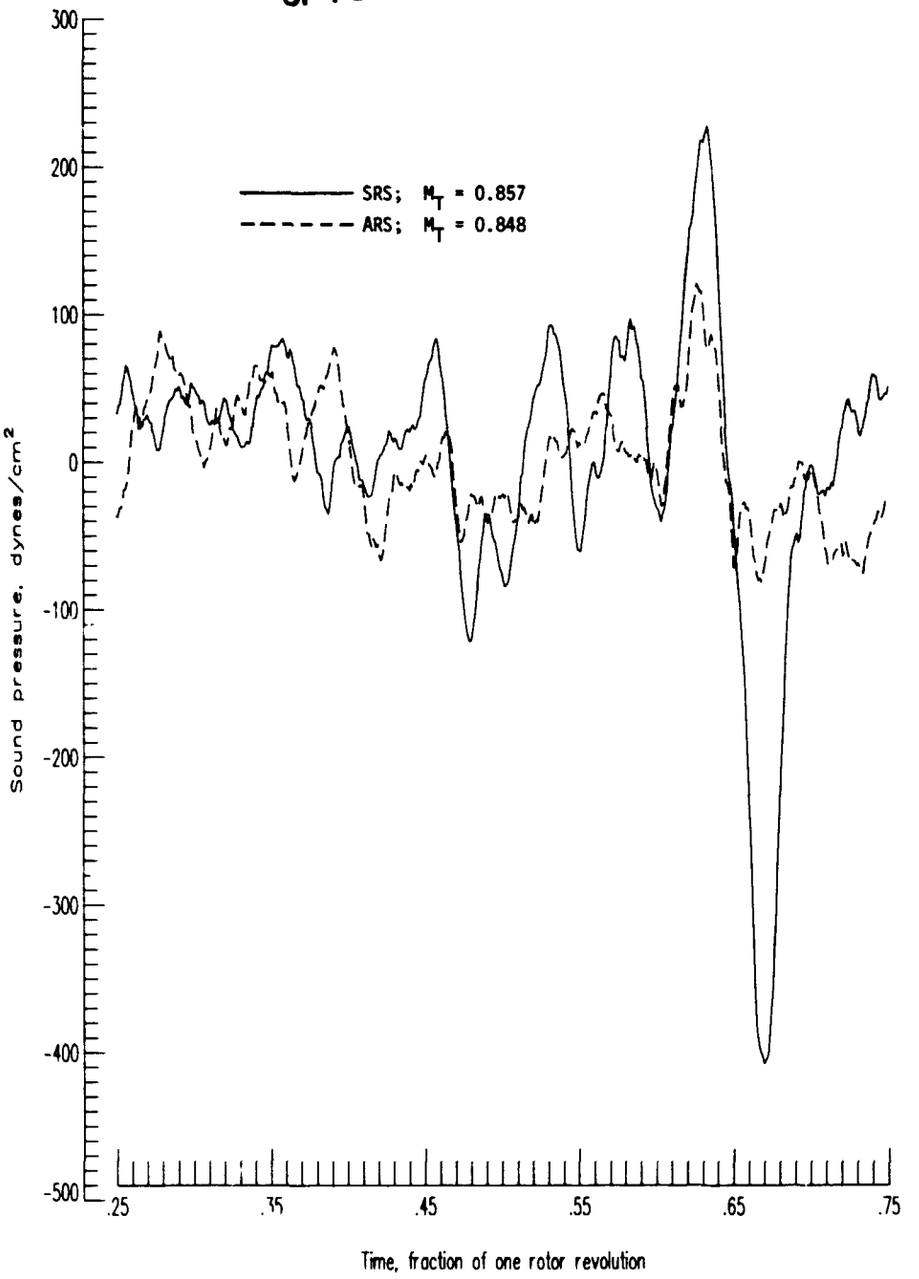

(d) Comparison of pressure-time histories for microphone 5.

Figure A5.- Continued.

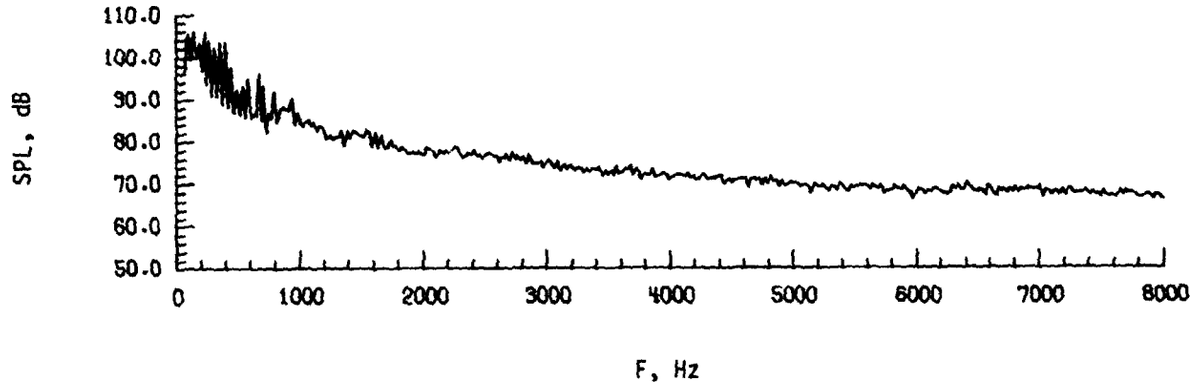

(e) Narrow-band spectrum for standard rotor system for microphone 5.

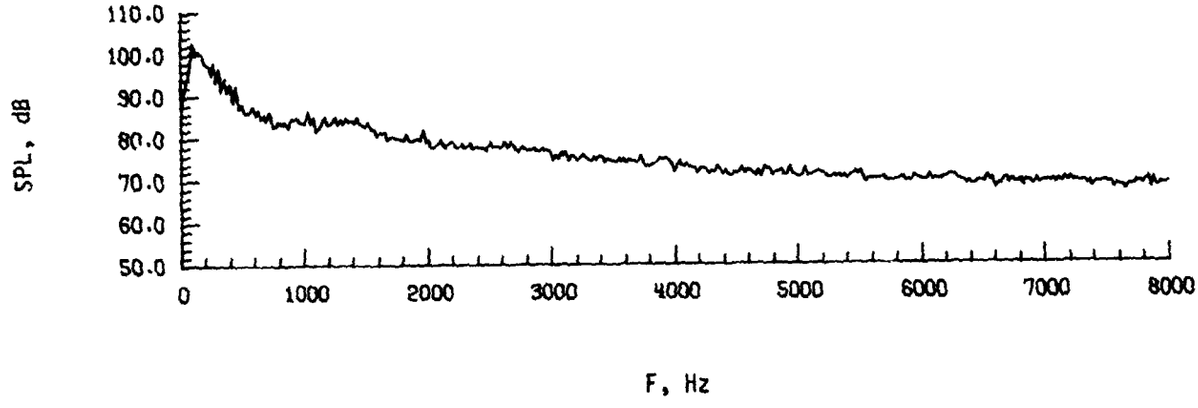

(f) Narrow-band spectrum for advanced rotor system for microphone 5.

Figure A5.- Concluded.

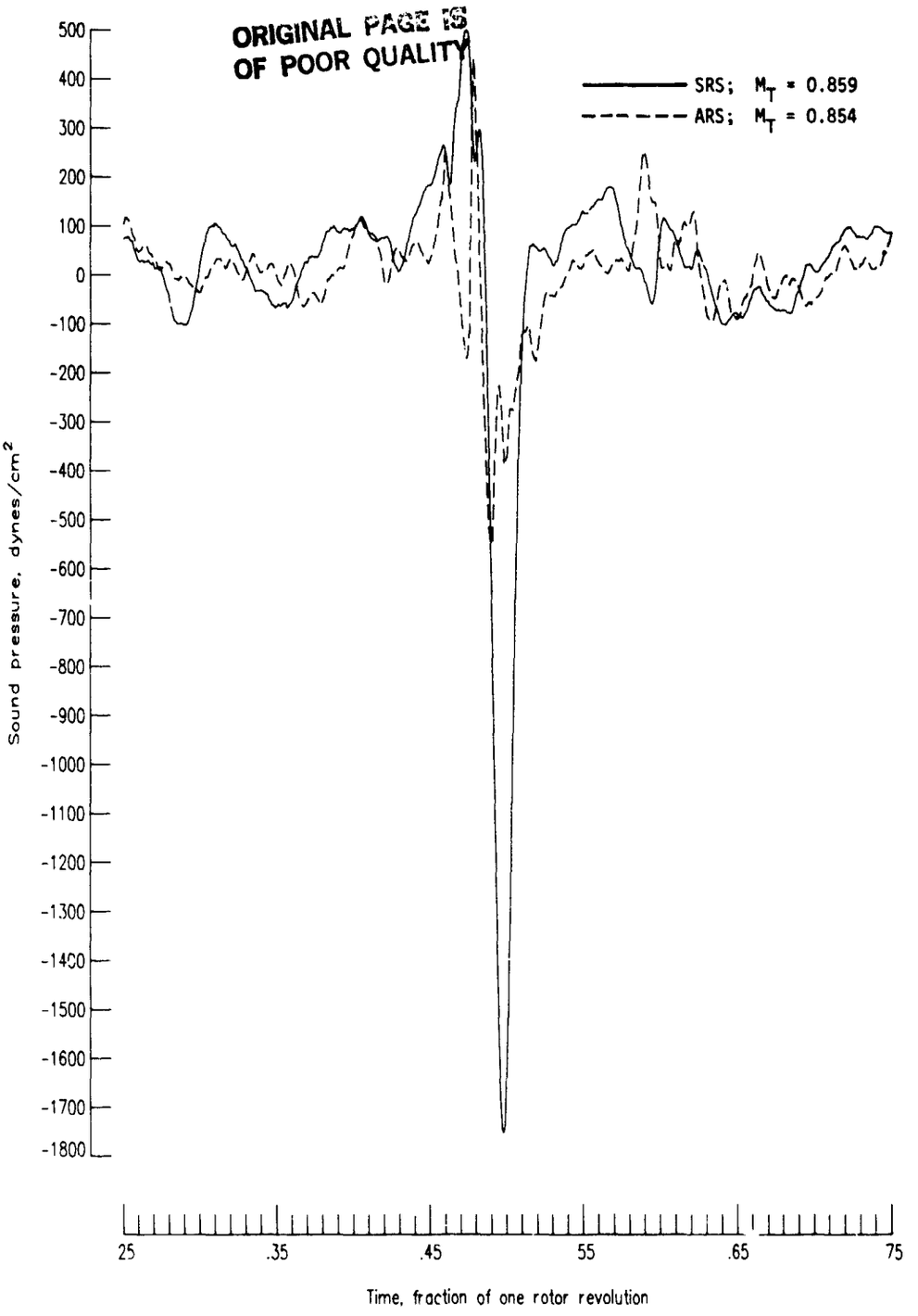

(a) Comparison of pressure-time histories for microphone 4.

Figure A6.- Effect of rotor system on noise signature generated by helicopter model at V_∞ = 105 knots.

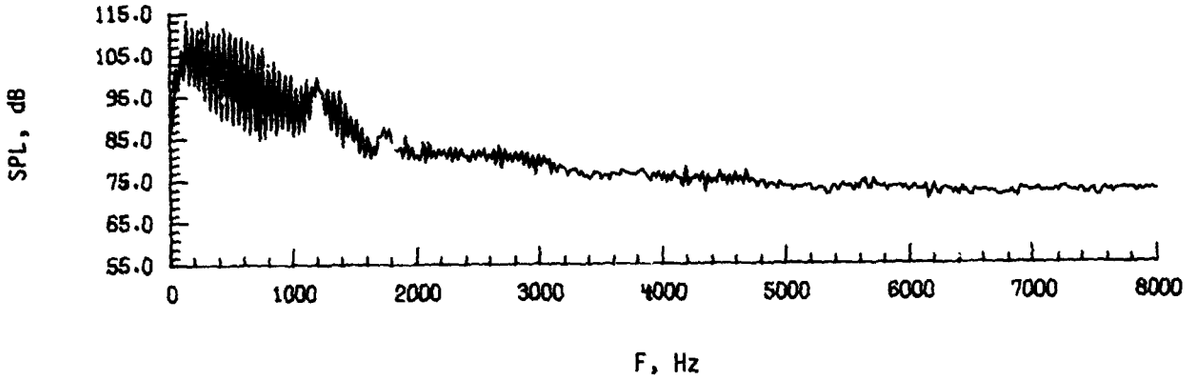

(b) Narrow-band spectrum for standard rotor system for microphone 4.

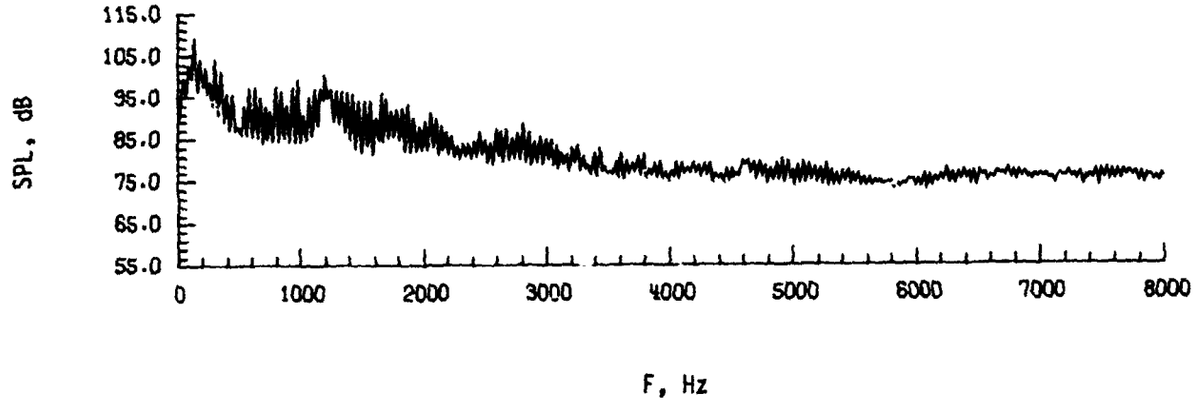

(c) Narrow-band spectrum for advanced rotor system for microphone 4.

Figure A6.- Continued.

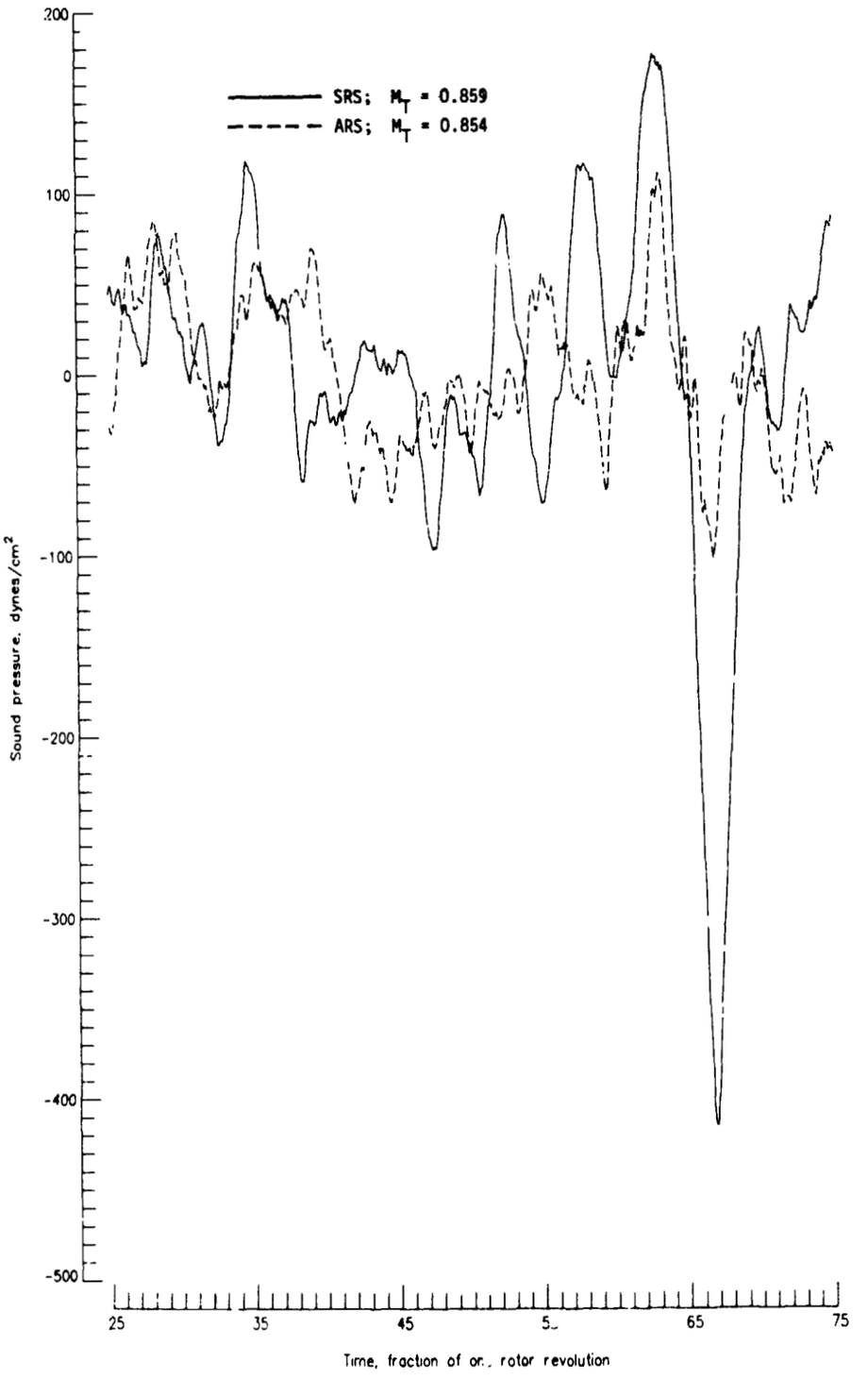

(d) Comparison of pressure-time histories for microphone 5.

Figure A6.- Continued.

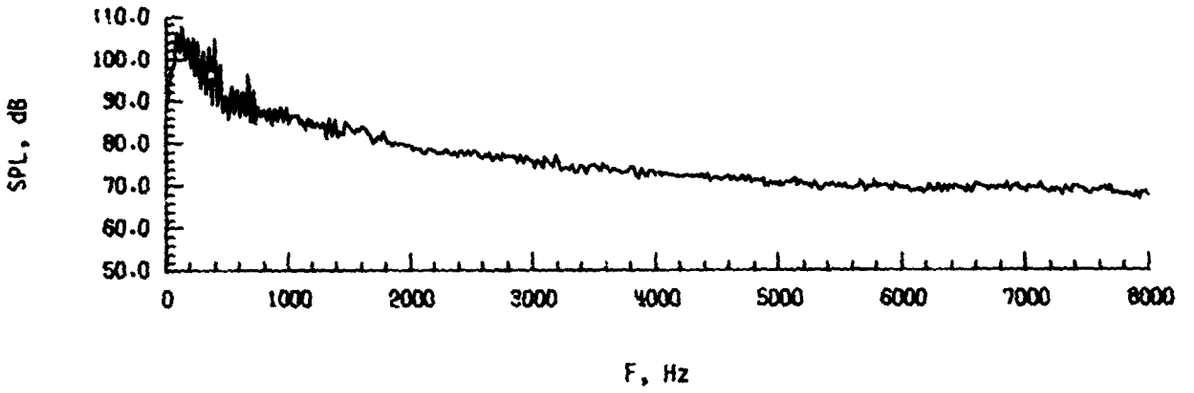

(e) Narrow-band spectrum for standard rotor system for microphone 5.

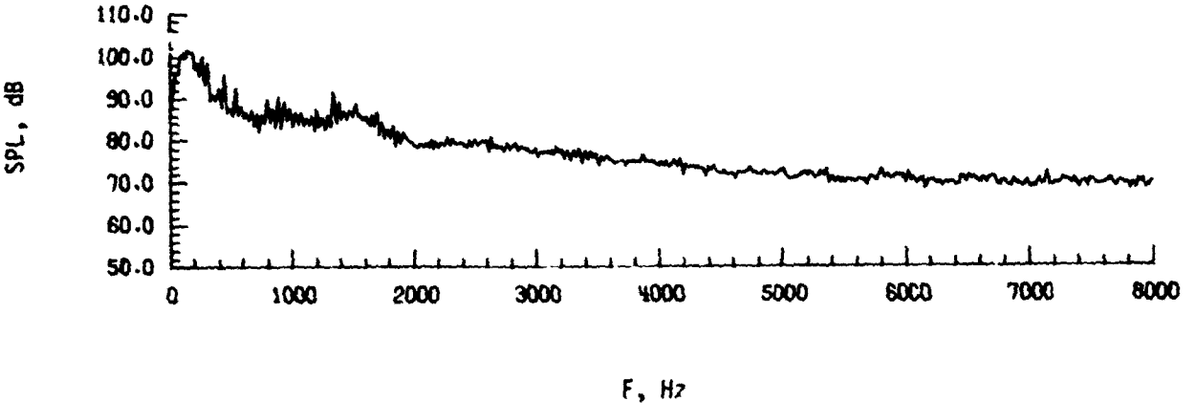

(f) Narrow-band spectrum for advanced rotor system for microphone 5.

Figure A6.- Concluded.

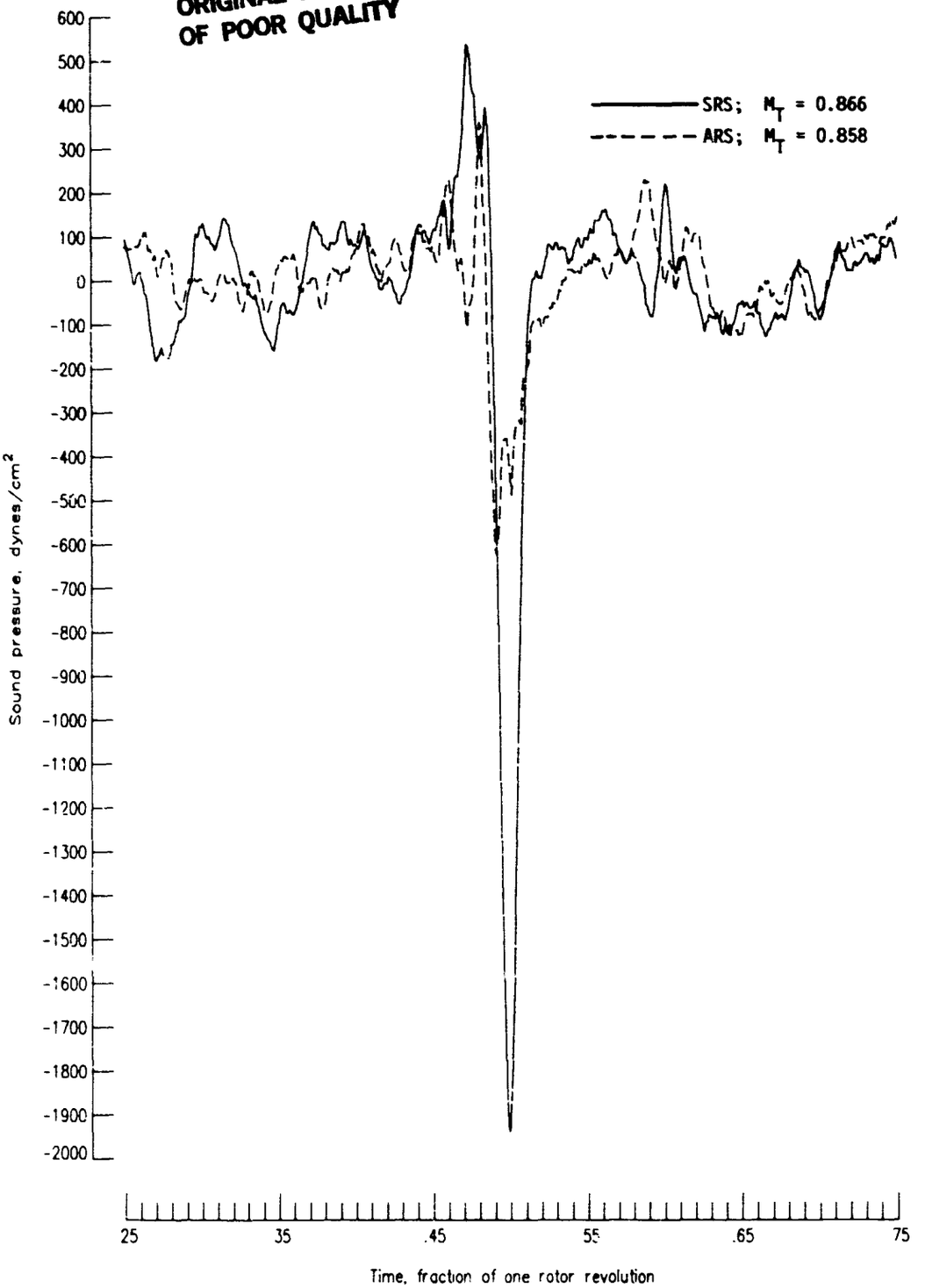

(a) Comparison of pressure-time histories for microphone 4.

Figure A7.- Effect of rotor system on noise signature generated by helicopter model at V_∞ = 110 knots.

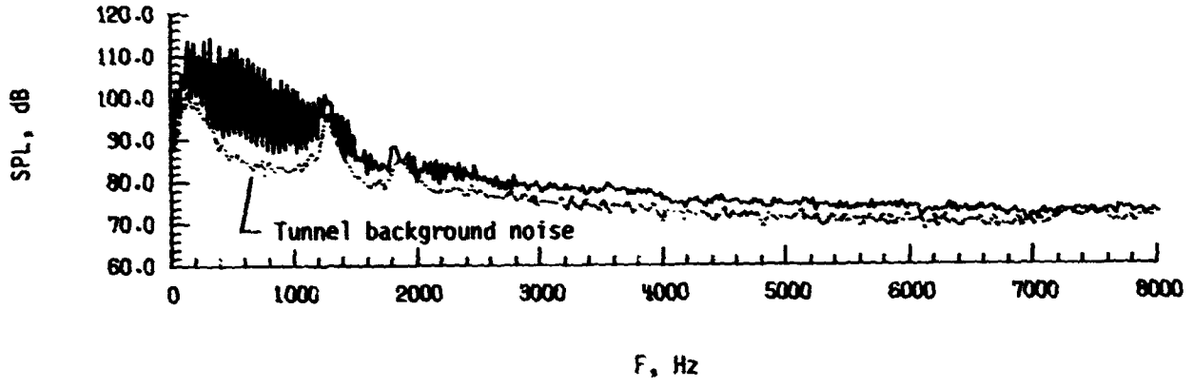

(b) Narrow-band spectrum for standard rotor system for microphone 4.

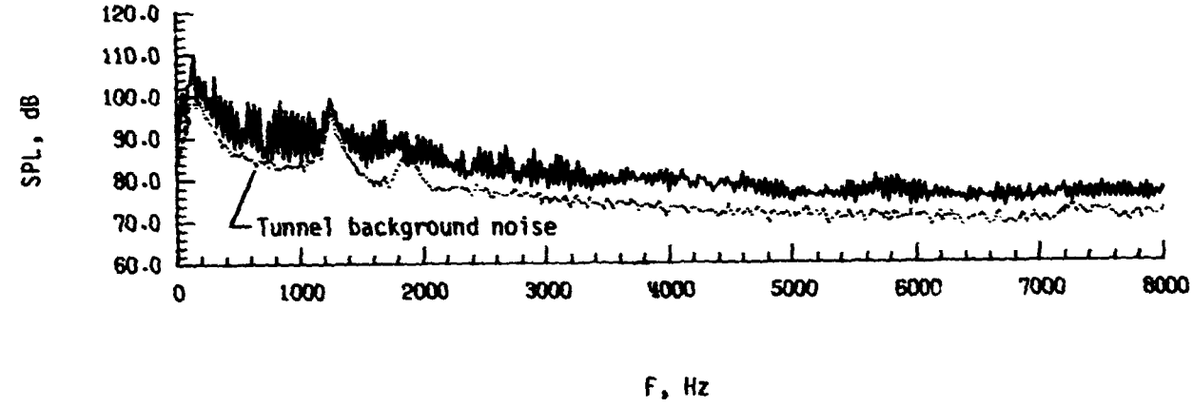

(c) Narrow-band spectrum for advanced rotor system for microphone 4.

Figure A7.- Continued.

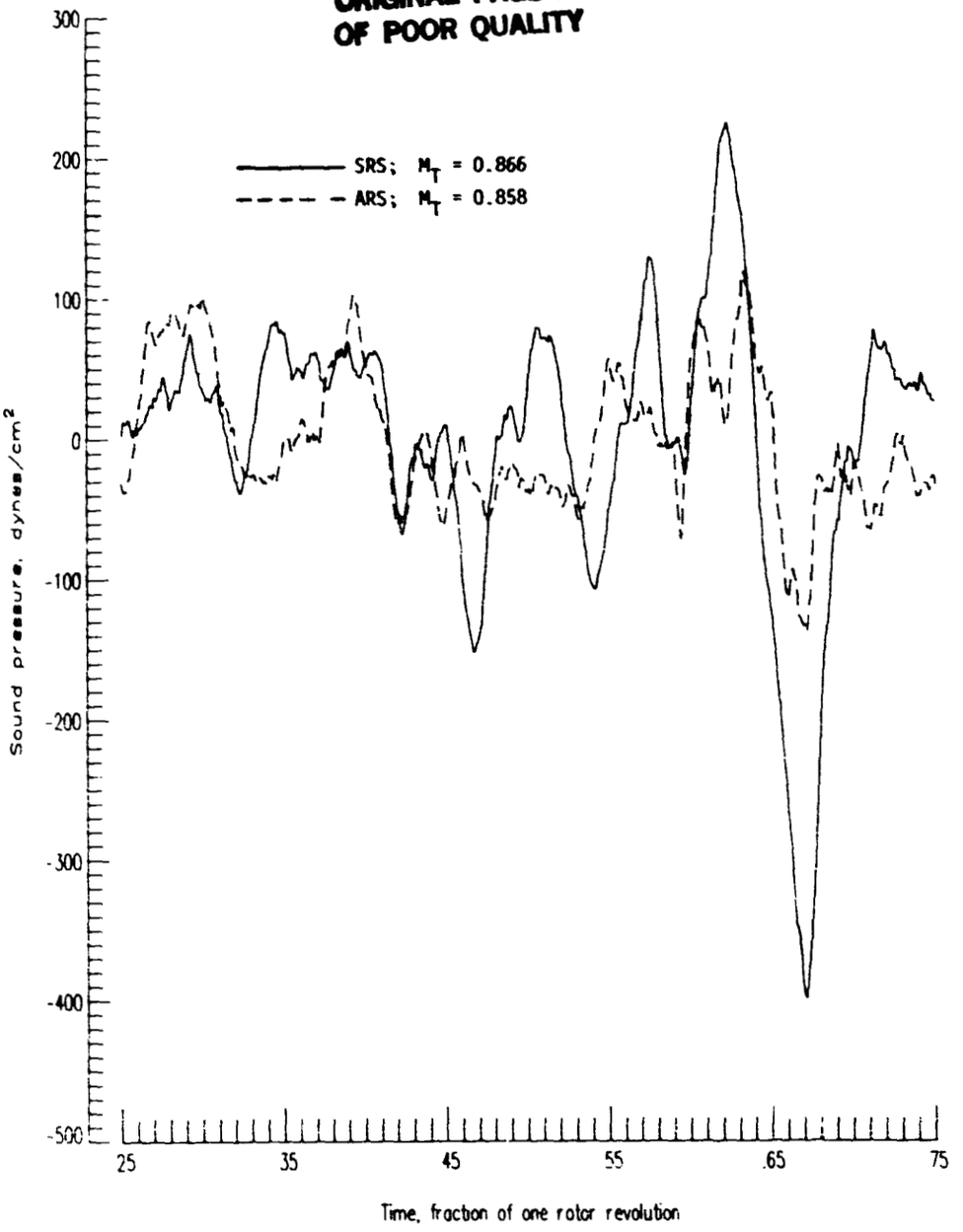

(d) Comparison of pressure-time histories for microphone 5.

Figure A7.- Continued.

ORIGINAL PAGE IS
OF POOR QUALITY

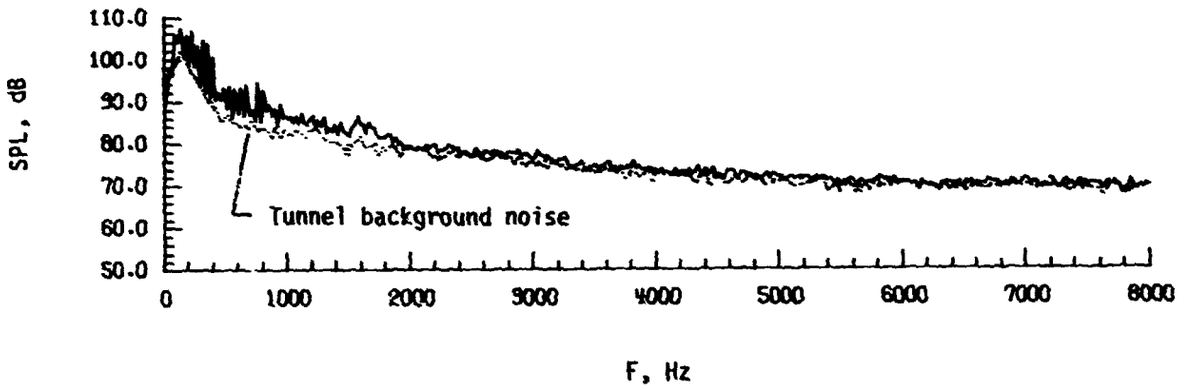

(e) Narrow-band spectrum for standard rotor system for microphone 5.

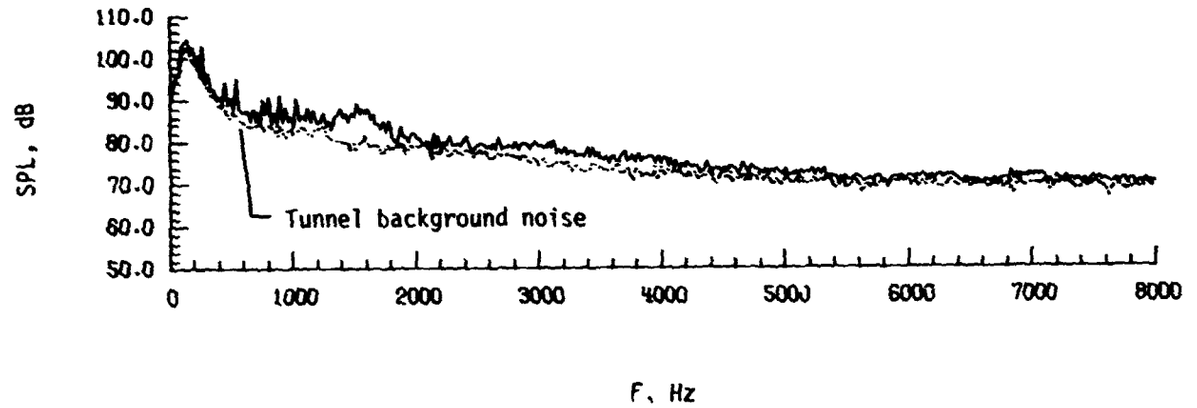

(f) Narrow-band spectrum for advanced rotor system for microphone 5.

Figure A7.- Concluded.

REFERENCES

1. Lowson, M. V.; and Ollerhead, J. B.: Studies of Helicopter Rotor Noise. USAAVLABS Tech. Rep. 68-60, U.S. Army, Jan. 1969.

2. Langenbucher, V.: Noise Phenomena With Helicopter Rotors and Possibilities of Noise Reduction. ESA TT-244, Feb. 1976.

3. Powell, Clemans A.; and McCurdy, David A.: Effects of Repetition Rate and Impulsiveness of Simulated Helicopter Rotor Noise on Annoyance. NASA TP-1969, 1982.

4. Hoad, Danny Robert: Helicopter Blade-Slap Noise Variation With Tip Vortex Modification. M.S. Thesis, The George Washington University, 1979.

5. Vause, C. R.; Schmitz, F. H.; and Boxwell, D. A.: High-Speed Helicopter Impulsive Noise. Preprint No. 1004, Proceedings of the 32nd Annual National V/STOL Forum, American Helicopter Soc., Inc., May 1976.

6. Farassat, F.: Theory of Noise Generation From Moving Bodies With an Application to Helicopter Rotors. NASA TR R-451, 1975.

7. Berry, John D.: Performance Testing of a Main Rotor System for a Utility Helicopter at 1/4 Scale. NASA TM-83274, AVRADCOM TR 82-B-3, 1982.

8. Hoad, Danny R.; and Conner, David A.: Acoustic Performance Evaluation of an Advanced UH-1 Helicopter Main Rotor System. Preprint 81-58, Proceedings of the 37th Annual Forum, American Helicopter Soc., May 1981.

9. Wilson, John C.: A General Rotor Model System for Wind-Tunnel Investigations. J. Aircr., vol. 14, no. 7, July 1977, pp. 639-643.

10. Bingham, Gene J.; Noonan, Kevin W.; and Jones, Henry E.: Results of an Investigation of Several New Rotorcraft Airfoils as Related to Airfoil Requirements Advanced Technology Airfoil Research, Volume II, NASA CP-2046, 1979, pp. 109-119.

11. Theobald, M. A.: Evaluation of the Acoustic Measurement Capability of the NASA Langley V/STOL Wind Tunnel Open Test Section With Acoustically Absorbent Ceiling and Floor Treatments. Rep. No. 3820 (Contract NAS1-14611-18), Bolt Beranek and Newman Inc., May 1978.

12. Schmitz, F. H.; and Boxwell, D. A.: In-Flight Far-Field Measurement of Helicopter Impulsive Noise. Preprint No. 1062, Proceedings of the 32nd Annual National V/STOL Forum, American Helicopter Society, Inc., May 1976.

13. Heyson, Harry H.: Use of Superposition in Digital Computers To Obtain Wind-Tunnel Interference Factors for Arbitrary Configurations, With Particular Reference to V/STOL Models. NASA TR R-302, 1969.

14. Singleton, Richard C.: On Computing the Fast Fourier Transform. Commun. ACM, vol. 10, no. 10, 1967, pp. 647-654.